COMPARING LOW-REDSHIFT COMPACT DWARF STARBURSTS IN THE RESOLVE SURVEY WITH HIGH-REDSHIFT BLUE NUGGETS

Michael L. Palumbo III,[1] Sheila J. Kannappan,[1] Elaine M. Snyder,[2] Kathleen D. Eckert,[3] Dara Norman,[4] Luciano Fraga,[5] Bruno Quint,[6] Philippe Amram,[7] Claudia Mendes de Oliveira,[8] Ashley Bittner,[9] Amanda Moffett,[10] David Stark,[11] Mark Norris,[1] and Nate T. Cleaves[1]

[1] University of North Carolina at Chapel Hill

[2] Space Telescope Science Institute

[3] University of Pennsylvania

[4] National Optical Astronomy Observatory

[5] Laboratório Nacional de Astrofísica Coordenadoria de Apoio a Ciencia

[6] Southern Astrophysical Research Telescope (SOAR)

[7] Laboratoire d'Astrophysique de Marseille

[8] Universidade de São Paulo

[9] North Carolina State University

[10] Vanderbilt University

[11] Kavli Institute for the Physics and Mathematics of the Universe

ABSTRACT

We identify and characterize compact dwarf starburst galaxies in the RESOLVE survey, a volume-limited census of galaxies in the local universe, to probe the extent to which these galaxies are analogous to "blue nuggets," a class of intensely star-forming compact dwarf galaxies at high redshifts. We compare the masses, star formation rates, stellar surface mass densities, projected axis ratios, and environmental contexts of our sample to expectations and observations of blue nuggets. We find that low-z blue nugget candidates in the RESOLVE survey are statistically analogous to their high-z counterparts, exhibiting masses, colors, and specific star formation rates (SSFR) consistent with past high-z observations. However, we find that the stellar surface mass densities of our low-z sample are on order 10^8 M$_\odot$kpc^{-2}, or about a dex lower than what is predicted and observed for high-z blue nuggets. Cosmological simulations and semianalytical models in recent years have suggested that blue nuggets form as the result of intense compaction events driven by either converging cosmic gas streams or wet minor mergers. In either formation scenario, simulations have additionally suggested that these galaxies should exhibit some degree of rotation along their minor axes and prolate morphology. We report 3D spectroscopy observations of four of low-z blue nugget analogues, from which we construct high-resolution velocity fields, examining the evidence for minor axis or otherwise misaligned rotation. We observe evidence for double nuclei in $\sim 85\%$ of our low-z blue nugget analogue sample, strongly favoring a merger origin for these objects. We additionally observe dynamically complex kinematics in the 3D spectroscopy observations with multiple components of rotation which are spatially consistent with the double nuclei detections, further suggesting recent wet minor mergers as the dominant formation mechanism for our low-z blue nugget analogues.

Keywords: galaxies: starbursts, evolution, interactions

1. INTRODUCTION

The first observations of a class of compact massive ($M_{star} \gtrsim 10^{11} M_\odot$) elliptical galaxies with suppressed star formation rates at $z \sim 2 - 3$ (van Dokkum et al. 2008; Ilbert et al. 2010) posed an evolutionary mystery. These galaxies, known technically as red quiescent galaxies (Barro et al. 2013) or colloquially as "red nuggets" (Damjanov et al. 2009; Newman et al. 2010), are extraordinarily compact with radii up to ~ 5 times smaller than typical galaxies of comparable mass in the low-z universe (Trujillo et al. 2007; Toft et al. 2007; Williams et al. 2014). The extreme stellar density of these objects has completely ruled out simple monolithic models of formation (as described in Eggen et al. 1962), which exclude significant structural evolution following initial galaxy assembly at very high redshifts (van Dokkum et al. 2008). Moreover, major merger models cannot account for the observed compactness of red nuggets, since these non-dissipative events preferentially scatter pre-existing stars to larger orbital radii, "puffing up" rather than compacting the resulting object (Naab et al. 2007; Naab & Ostriker 2009).

More recently, cosmological simulations (such as in Ceverino et al. 2015; Tacchella et al. 2016) have suggested that minor, wet mergers favorably produce remnants with ultra-compact cores as a result of the dissipative nature of the gas allowing for angular momentum loss (Khochfar & Silk 2006; Hopkins et al. 2008). Indeed, complementary observations have pinned a class of compact star-forming dwarf galaxies known as "blue nuggets" as suitable evolutionary progenitors for red nuggets (Patel et al. 2013; Barro et al. 2013; Nelson et al. 2014). Using a toy model, Dekel & Burkert (2014) analytically demonstrate that inflow from smooth cosmic streams and minor wet mergers generate sufficient angular momentum loss to account for the extraordinary compactness of red nuggets. They show the extreme gas inflow ignites a chain of events, culminating in violent disk instability, contraction, and rapid star formation so long as the rate of dissipative gas inflow exceeds the rate of star formation in the central regions of the galaxy, creating a blue nugget. Without a fresh supply of gas, these blue nuggets eventually quench, evolving into the observed red nugget phase.

Analyses of the observed projected ellipticities of galaxies at $z > 1$ have shown that the distribution of galaxy morphologies at at high redshift are predominately triaxial (Law et al. 2012). Follow up analyses by Chang et al. (2013) and van der Wel et al. (2014) have together demonstrated that the oblate fraction of galaxies with $M_{star} < 10^{10.5} M_\odot$ increases with cosmic time, and that most galaxies with $M_{star} \sim 10^{8.5} - 10^{9.5} M_\odot$

at $z \sim 1 - 2$ are prolate, suggesting that the evolution from the blue nugget phase to the red nugget phase, as outlined by Dekel & Burkert (2014), should also include an evolution in morphology. Indeed, cosmological simulations of blue nuggets have shown that the minor merger formation scenario should create prolate objects (Jing & Suto 2002; Bailin & Steinmetz 2005; Allgood et al. 2006), whose major axes are preferentially aligned with the larger filamentary structure of the cosmic web in which they are embedded (Codis et al. 2015; Laigle et al. 2015). Additional simulations performed by Tomassetti et al. (2016) have shown torques induced by the dark matter (DM) halo during the gas compaction event are capable of elongating the stellar system into a prolate shape. Simulations conducted by Tomassetti et al. (2016) and Ceverino et al. (2015) both reveal that blue nuggets tend to display some degree of characteristic rotation along their minor axes.

Tacchella et al. (2016) show that blue nuggets undergo successive cycles of compaction and quenching, so long as there is a fresh supply of gas to replenish central star formation. They predict that this "self-regulated evolution" ultimately tends toward a red nugget when hot halo quenching dominates at virial mass $M_{vir} \sim 10^{11.5}$, corresponding to a stellar mass on order $M_{star} \sim 10^{10}$ at most. Dekel & Burkert (2014) surmise that the self-regulated evolution of blue nuggets is dependent upon "fast-mode" growth, which allows for extremely rapid star formation, mass accretion, and ultimately rapid quenching driven by hot halos. In the opposite case of "slow-mode" growth, slower gas accretion regulates the rapid formation of stars, slowing progress across the red sequence. The rapid appearance of a red sequence on the scale of ~ 0.7 Gyr, as shown by Barro et al. (2013), is consistent with the relatively rapid quenching characteristic of fast-mode accretion.

At low redshift, Stark et al. (2013) show that galaxies evolve along a "fueling diagram," a plot of H_2/HI gas ratio versus blue centeredness that may reflect analogous cycles of gas accretion and depletion. This fueling diagram has three branches, two of which are primarily populated by blue E/S0s and blue compact dwarfs (BCDs). Patterns of total gas content and stellar population age along these two branches suggest cyclical evolution characterized by rapid star formation, gas depletion, and disk regrowth. The existence of such cyclical evolution cycles at low-z suggests that the self-regulated evolution of blue nuggets may still be possible even with the lower fresh gas inventory of the present-day universe.

While mechanisms for fresh gas accretion, mass growth, and star formation clearly exist in the present-day universe, as demonstrated by Stark et al. (2013),

it is currently unclear whether the fast-mode accretion, which is dependent upon very high gas fractions and therefore preferential to the high redshifts, can occur in the present day universe. Indeed, Dekel & Burkert (2014) calculate that the fraction of galaxies which become blue nuggets depends primarily upon the fraction of cold gas mass with respect to baryon mass, a parameter which decreases dramatically with cosmic time. Observations by van der Wel et al. (2014) correspondingly show that the fraction of prolate galaxies with $M_{star} \lesssim 10^{9.5}$, namely blue nuggets, decreases dramatically from $z = 2$ to $z = 0$. However, this fraction is non-vanishing at $z = 0$ despite its strong dependence on cosmic time. The non-zero prolate galaxy fraction combined with the observation of massive compact quiescent galaxies (i.e. red nuggets) at intermediate redshifts as low as $z \sim 0.1$ by Damjanov et al. (2015) suggests the possibility of fast-mode accretion and quenching occurring in the intermediate- and low-z universe.

We therefore desire to examine the existence and nature of blue nuggets in the low-z universe. Is there a population of compact starburst dwarfs in the present-day universe analogous to high-z blue nuggets? Do they exhibit prolate morphology and rotation along their minor axes? Do they form by the same two mechanisms proposed at high-z (i.e. wet minor mergers and colliding cosmic streams)?

To answer these questions, we turn to the REsolved Spectroscopy Of a Local VolumE (RESOLVE) Survey[1], a volume-limited census of galaxies in the local universe, whose statistical completeness and low mass floor is ideal for identifying and characterizing a population of galaxies nearly a full dex lower in mass than the Barro et al. (2013) blue nugget sample. We present the identification of a population of 35 low-z blue nugget candidates in RESOLVE. We examine the key statistical features of the low-z candidate sample, comparing to high-z blue nuggets in order to characterize the exact relationship between the present-day and distant-past populations. By studying the star formation rates and morphologies of the low-z blue nugget candidates, we probe the evolutionary relationship of these objects to their high-z counterparts. By studying the distributions of nearest neighbor distances and rate of double nucleus occurrence, we examine the possible formation mechanisms of the low-z blue nugget candidates, and therefore the nature of fast-mode accretion in the present-day universe.

In order to further address the formation history of the low-z blue nugget candidate population, we use follow-up 3D spectroscopy to probe the internal structure and kinematics of four candidate galaxies. We compare the structure of these individual galaxies to expectations from high-z simulations by:

i. constructing and modeling velocity fields to search for minor-axis, misaligned, or multi-component rotation as revealed in simulations by Ceverino et al. (2015) and Tomassetti et al. (2016)

ii. creating continuum and Hα flux maps to search for or confirm double nuclei as a probe of the wet minor merger mechanism of fast-mode growth

This work is laid out as follows. In section 2 we describe the RESOLVE survey, our sample selection, and the follow-up 3D spectroscopy data. In section 3 we discuss our analysis of the 3D spectroscopy data, including velocity fields, continuum maps, and Hα line flux maps. In section 4 we examine the formation and environments of the low-z blue nugget candidate sample, in addition to making statistical comparisons to the literature high-z blue nugget populations. In section 5 discuss the relationship between the low-z and high-z population, examining whether the present-day candidates are actually blue nuggets or simply analogous, but not identical, entities. Finally, in section 6 we summarize our findings.

We assume a standard ΛCDM cosmology with $\Omega_m = 0.3$, $\Omega_\Lambda = 0.7$, and $H_0 = 70$ km s^{-1} Mpc^{-1} for distance measurements and other derived quantities in this work.

2. DATA

2.1. The RESOLVE Survey

For this work, we use the RESOLVE (REsolved Spectroscopy of a Local VolumE) survey, a volume-limited census of galaxies in the local universe with the goal of accounting for baronyic and dark matter mass within a statistically complete subset of the $z \sim 0$ galaxy population. As a result of the volume-limited nature, RESOLVE is ideal for examining the properties of the full low-z blue nugget candidate population without the statistical completeness corrections endemic to flux-limited surveys. Moreover, the low mass floor of RESOLVE allow us to probe deeper into the prolate mass regime of $M_{star} < 10^{9.5}$ observed by van der Wel et al. (2014), as opposed to the $M_{star} > 10^{10}$ mass limit of Barro et al. (2013) which lies above the prolate mass regime.

2.1.1. Survey Definition and Ancillary Data

RESOLVE covers two equatorial strips, denoted RESOLVE-A and RESOLVE-B, which together enclose a volume of $\sim 52,100$ Mpc^3 in the $z \sim 0$ universe (Eckert et al. 2015). Both sections of the survey are
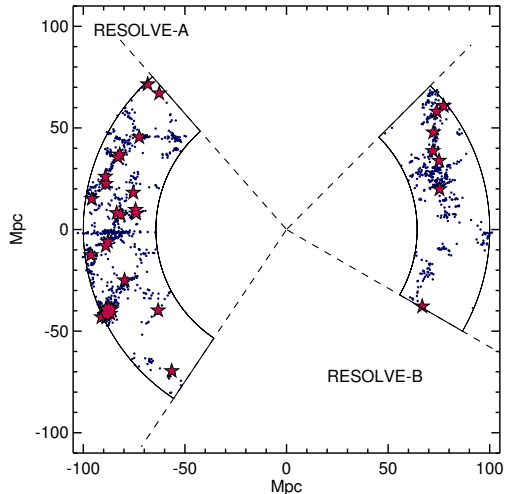
Figure 1. RESOLVE survey footprint with low-z blue nugget candidates (see section 2.1.2) highlighted as red stars.

bounded in Local Group-corrected heliocentric velocity from $V_{LG} = 4500 - 7000$ km s^{-1}. To avoid situations where peculiar velocities may affect survey membership, group (rather than individual) redshifts are used to decide final survey membership. RESOLVE is contained within the SDSS footprint and uses the SDSS redshift survey to build survey membership. In addition to redshifts measurements obtained from RESOLVE observations (Kannappan et al. 2018, in prep.), we include additional redshifts from a number of archival sources: the Update Zwicky Catalog (Falco et al. 1999), Hyper-Leda (Paturel et al. 2003), 6dF (Jones et al. 2009), 2dF (Colless et al. 2001), GAMA (Driver et al. 2011), and ALFALFA (Haynes et al. 2011).

As shown in Kannappan et al. (2013) and Eckert et al. (2016), RESOLVE-A is complete down to $M_{r,tot} = -17.33$, which roughly corresponds to a baryonic mass completeness limit of $\log(M_{bary}/M_\odot) = 9.3$. For the slightly deeper RESOLVE-B, the luminosity completeness limit of $M_{r,tot} = -17.0$ corresponds to a baryonic mass completeness limit of $\log(M_{bary}/M_\odot) = 9.1$ and a stellar mass completeness limit of $\log(M_{star}/M_\odot) = 8.7$.

As described in Eckert et al. (2015) RESOLVE employs reprocessed photometric data from the UV through NIR. RESOLVE data in the optical *ugriz* comes from SDSS (Aihara et al. 2011), NIR *JHK* from 2MASS (Skrutskie et al. 2006) and/or *YHK* from UKIDSS (Hambly et al. 2008), and NUV from *GALEX* (Morrissey et al. 2007). The reprocessed RESOLVE photometry improves on SDSS pipeline photometry as the result of improved sky subtraction, improved elliptical apertures generated from summed high signal-to-noise

ratio (SNR) *gri* images, and the use of non-parametric models of magnitude extrapolation (among other factors discussed in detail in Eckert et al. 2015). RESOLVE stellar masses are calculated from the SED modeling code described in Kannappan & Gawiser (2007) and Kannappan et al. (2013), which uses photometric data from up to 10 bands to provide robust estimates of stellar mass. The HI masses and upper limits are obtained from deep, pointed observations with the GBT and Arecibo telescopes supplementing the blind 21 cm ALFALFA survey (Haynes et al. 2011), and are calculated as in Kannappan et al. (2013) and Stark et al. (2016). Group finding is performed using the Friends-of-Friends algorithm as described in (Berlind et al. 2006) and justified in (Eckert et al. 2016). Group halo masses are assigned by using halo abundance matching between identified groups and the theoretical halo mass function of Warren et al. (2006), as described in Berlind et al. (2006) and Moffett et al. (2015). RESOLVE de-extincted central Hα fluxes are obtained by Balmer decrement measurements and foreground extinction corrections of SDSS central flux measurements using the Milky Way extinction curve of O'Donnell (1994) as given by McCall (2004).

2.1.2. *Sample Definition*

We identify a sample of 35 blue nugget candidate galaxies in the RESOLVE Survey. Guided by the observed and simulated properties of high-z blue nuggets in literature, we have constrained our candidate blue nuggets to a region of parameter space containing highly compact, possibly prolate galaxies in the dwarf mass regime. We implement selectors in stellar mass, morphology, color, and specific star formation rate (SSFR):

- Theoretical study (Ceverino et al. 2015) and observations (van der Wel et al. 2014) of prolate galaxies has shown that hot halo quenching begins to shut down cosmic gas accretion in blue nuggets above stellar mass $\log(M_{star}/M_\odot) \sim 9.5$. We select objects below this mass threshold. Our selection also includes an explicit mass floor, corresponding to the completeness limit of the RESOLVE survey: $\log(M_{bary}/M_\odot) = 9.3$ $M_\odot$ and $\log(M_{bary}/M_\odot) = 9.1$ respectively for RESOLVE-A and -B, where M_{bary} is the combined mass of cold gas and stars.

- As shown in high-z simulations, blue nuggets are expected to be compact, prolate ellipsoids. To select on morphology, we use the μ_Δ parameter developed by Kannappan et al. (2013) as quantita-

(a)

(b)

(c)
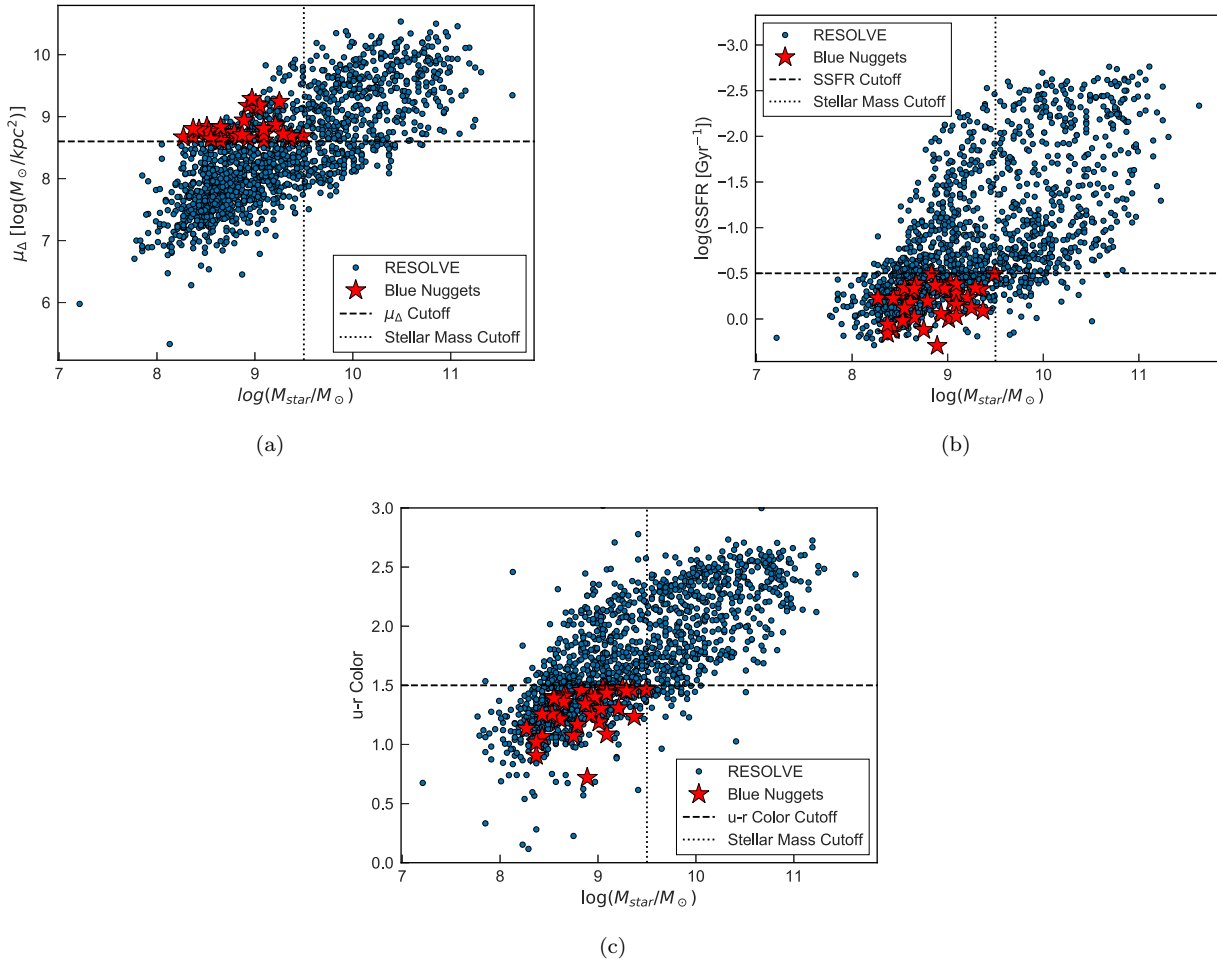
Figure 2. Selection plots for low-z blue nuggets. (a) For their mass, blue nugget candidates are among the most compact objects in the RESOLVE survey, reflecting the intense compaction events that have driven their starbursts. (b) The selection of $\log(\text{SSFR } [\text{Gyr}^{-1}]) > -0.5$, as in the Barro et al. (2013) sample, isolates some of the most intense starbursts in RESOLVE. Note that the y-axis is inverted for the sake of consistency with the Barro et al. (2013) standard. (c) Blue nugget candidates sit well within the blue sequence of RESOLVE.

tive surrogate for Hubble type[2]. Restricting our sample to $\mu_\Delta > 8.6$ limits our sample to bulged disk and spheroid-dominated galaxies with high degrees of concentration of central star formation (Figure 2a).

- Dekel & Burkert (2014) show that blue nuggets should be found on the blue end of the blue sequence. To select galaxies in the blue sequence of RESOLVE, we implement a color restriction of $u - r < 1.5$.

---

[2] μ_Δ combines the overall stellar surface mass density with a stellar surface mass density contrast term: $\mu_\Delta = \mu_{90} + 1.7\Delta_\mu$. The contrast term Δ_μ is expressed as the difference between the stellar surface mass densities within the 50% light radius and between the 50% and 90% light radii. See Kannappan et al. (2013).

- Blue nuggets are impressive starbursts as a result of the intense gas compaction in their centers. To select galaxies undergoing starbursts similar to those at high redshift, we impose a specific star formation rate limit of $\log(\text{SSFR } [\text{Gyr}^{-1}]) > -0.5$ as in Barro et al. (2013). Accordingly, we find that this restriction simultaneously selects RESOLVE galaxies whose de-extincted central Hα fluxes lie in the upper ~50th percentile (Figure 3, right).

2.2. 3D Spectroscopic Data

For this work, we use supplementary 3D spectroscopic data obtained from the Gemini South Multi-Object Spectrograph Integral Field Unit (GMOS IFU), the SOAR Integral Field Spectrograph (SIFS), and the SOAR Adaptive Module Fabry-Pérot (SAM FP). Both the GMOS IFU and SIFS use fiber-fed lenslet arrays to
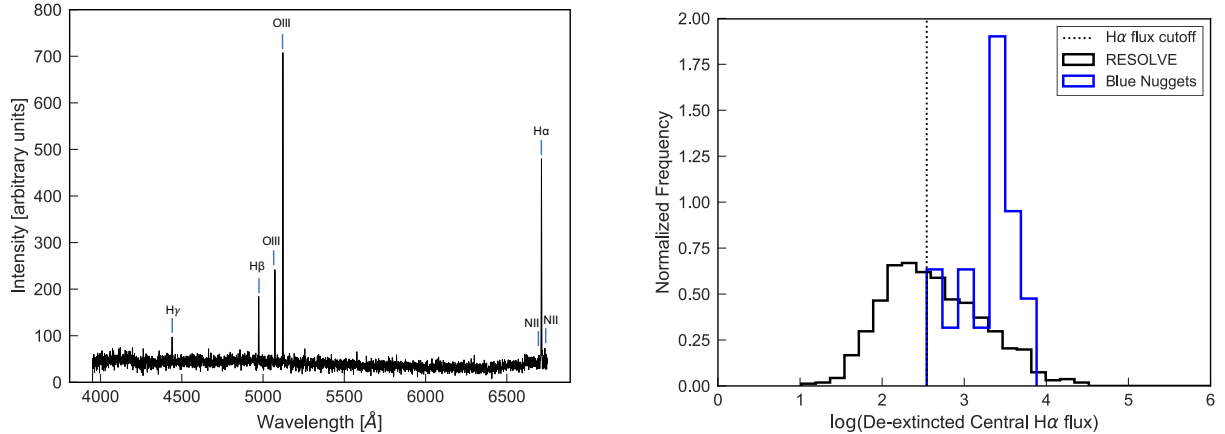
Figure 3. **Left: SIFS spectrum for *rs1103* displaying dominant Hα and [OIII] emission lines typical of blue nugget spectra.** Powerful [OIII] emission lines are strongly indicative of metal-poor gas. The strong Hα emission signifies intense star formation, which is corroborated by the strong blue color in the photometry. **Right: Distributions of de-extincted Hα fluxes for RESOLVE and for compact blue dwarf galaxies.** Our selection on log(SSFR [Gyr^{-1}]) > −0.5 implicitly selects RESOLVE galaxies with de-extinced central Hα fluxes in the upper 50th percentile.

sample galaxy spectra at each lenslet position. Compared to traditional longslit spectroscopy, integral field spectroscopy allows us to easily construct spatially-resolved velocity fields of extended objects by sampling object spectra at ∼ 1000 discrete points (in the case of the GMOS IFU) and arranging these spectra into "pseudoslits" whose light is dispersed onto the detector. In a different vein, SAM FP uses an etalon to image a target at discrete wavelengths within a narrow spectral range. In comparison to IFU instruments, the SAM FP is able to sample at a much higher spatial frequency at the expense of spectral range.

To extract spatially-resolved velocity and continuum information, we rely primarily upon the strong Hα emission line. Depending on the wavelength range of the instrument setup, we may also use the [NII] doublet, the [OIII] doublet, and Hβ. In all cases, the field-of-view must cover the full spatial extent of emission for the galaxy. In several cases, this has necessitated spatial tiling of exposures. The centroiding accuracy of the Hα line should be ∼ 5 km/s at the half-light radius of galaxy to avoid unacceptable errors in velocity calculations. Table 1 contains a summary of the instrument setups.

In order to probe the dynamical properties of our objects, we require reduced data cubes with spatial information in the x-y plane, and spectral information along the z-axis. From these we obtain spatially resolved velocity fields, continuum maps, and Hα flux maps, as described in section 3.1. These plots serve as our primary evidence for i) minor-axis or misaligned rotation and ii) double nuclei detection.

For the GMOS IFU data we have developed the Gemini Reduction Pipeline in order to efficiently and accurately transform the two-dimensional observational data into three-dimensional data cubes. For a description of the Gemini reduction process, see Appendix A. Since we obtained the SIFS and SAM FP data in science verification (SV) time, the respective SV teams performed the data reduction into data cubes. The SAM FP reduction was performed as described in Mendes de Oliveira et al. (2017), including calibrations analogous to the GMOS IFU reduction (e.g. bias subtraction, wavelength calibration, cosmic ray rejection, etc.). We additionally perform astrometrical calibration on the SAM FP data by matching field stars in the Aladin Sky Atlas desktop program (Bonnarel et al. 2000). The SIFS data reduction is performed in a process largely analogous to the GMOS IFU reduction process (including bias subtraction, flat fielding, cosmic ray removal, etc.). However, an additional side-step calibration is required to extract the fiber spectra due to the dense packing of information along the spatial direction on the CCD, which would otherwise lead to severe fiber "cross-talk" in the extracted spectra (private communication with Luciano Fraga, Fraga et al. in prep).

2.3. *DECaLS*

We supplement our analysis of low-z blue nugget candidate formation scenarios via double nucleus detection (section 4.2.1) with photometry from Data Release 5 (DR5) of the Dark Energy Camera Legacy Survey (DE-CaLS)[3].

---

[3] http://legacysurvey.org/decamls/

Table 1. Summary of spectroscopic instrument setups.

	GMOS IFU	SIFS	SAM FP
spectral range	5500 - 6900 Å	4000 - 6800 Å	varies[a]
lines of interest	Hα, [NII]	Hβ, [OIII], HαNII]	Hα
grating	B600	700B	N/A
filter	r-G0326	none	LAM-M13, LAM-M15
pseudoslits	2 slits	1 slit	N/A
field of view	5" × 7"	7.8" × 15"	3′ × 3′
Spectral Resolution	1688	4200	∼ 12000[a]
Program ID	GS-2013B-Q-51	N/A	N/A
Observations	*rf0250, rf0266*	*rs1103*	*rf0250, rf0266, rs0804*

[a]The wavelength range and spectral resolution of SAM FP are dependent on the free spectral range (FSR). The central wavelength of the FSR is chosen to correspond to the mean heliocentric velocity of the observed object. See Mendes de Oliveira et al. (2017).

DECaLS images are initially calibrated using the DE-Cam Community Pipeline[4] before being processed by The Tractor (Lang et al. 2016), which creates probabilistically motivated models and the residual images used in section 4.2.1. The Tractor approximates galaxy profiles with mixture-of-Gaussian models (Hogg & Lang 2013) which are fit via χ^2 minimization using the sparse least squares solver from the SciPy package.

3. METHODS

3.1. *Analyzing Spectroscopic Data Cubes*

The ultimate product of the 3D spectroscopy reduction process is a data cube that contains spatial data on the xy-plane and spectral data on the z-axis. Since the data cubes, regardless of instrument, are in principle the same, we apply the same analysis methods to data cubes from all three instruments. We extract three key pieces of information from these data cubes: velocity fields, continuum maps, and Hα line flux maps.

We use the *mpfit* algorithm (Markwardt 2009), translated into Python by Mark Rivers, to perform a non-linear least-squares fit of the spectra with a Gaussian line model. For SAM FP, we fit a single Gaussian to the Hα line. For GMOS IFU, we fit three Gaussian curves to the [NII] and Hα lines. For SIFS, we fit the [OIII] doublet, Hβ, the [NII] doublet, and Hα. For a given

instrument, the total model spectrum is represented as the sum of individual line models and the continuum level. For a generic single line with non-zero continuum level, our model takes the form:

$$I_{obs} = \frac{I_{rest_{peak}}}{\sqrt{2\pi\sigma^2}(1+z)} \exp\left(\frac{-(\frac{\lambda_{obs}}{(1+z)} - \lambda_{rest})^2}{2\sigma_{rest}^2} \right) + I_{cont} \quad (1)$$

where I_{obs} is the observed intensity a function of wavelength, $I_{rest_{peak}}$ is the peak rest frame intensity of a given line, σ_{rest} is the rest frame Gaussian sigma of the line, I_{cont} is amplitude of the continuum, and z is the net redshift (including cosmological, peculiar, and rotational redshifts, as in Equation 2). This fit is performed for every spectrum in the cube, and the fitted model parameters are recorded. Figure 4 shows an example of a fit spectrum.

3.1.1. *Velocity Fields*

To produce velocity fields, we assume that the net redshift z is the product of internal rotation, peculiar motion, and cosmological redshift components:

$$1 + z = \left(1 + \frac{v_{rot}}{c}\right)\left(1 + \frac{v_{pec}}{c}\right)\left(1 + \frac{v_{cosm}}{c}\right) \quad (2)$$

However, since we cannot disentangle peculiar and cosmological redshifts, we further assume that the peculiar and cosmological terms can be consolidated as such:

$$1 + z = \left(1 + \frac{v_{rot}}{c}\right)\left(1 + \frac{v_{hel}}{c}\right), \quad (3)$$
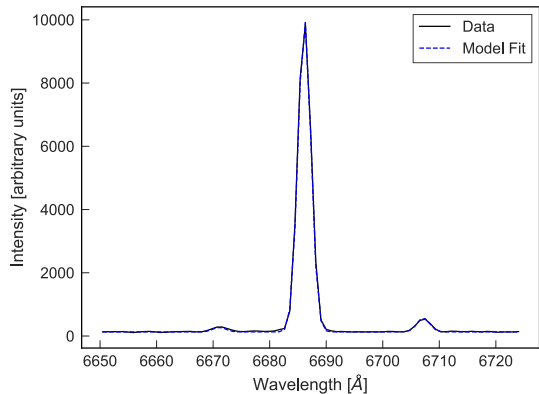
Figure 4. Example spectrum extracted from GMOS IFU data for *rf0250* with Gaussian fit. The Hα emission line is plotted in blue, with the best-fit triple-Gaussian model overplotted in red. We obtain higher centroiding, and therefore velocity, accuracy by fitting to the [NII] and Hα lines, as opposed to just Hα.

where v_{hel} is the recessional velocity of the galaxy in the heliocentric reference frame, estimates of which are obtained from redshift measurements as described in section 2.1.1. Rearranging Equation 3, we calculate the internal rotation velocity as:

$$v_{rot} = c \left((1 + z) \left(1 + \frac{v_{hel}}{c} \right)^{-1} - 1 \right), \qquad (4)$$

where z is obtained from the model fit in Equation 1.

We iteratively improve our measurement of v_{rot} by re-measuring v_{hel} as the average velocity in the high SNR region of the initial velocity map. In the future, we may further improve our estimation of v_{hel} by employing the probable minimum/maximum technique described in Kannappan et al. (2002). We find that this method produces compatible results for observations from separate instruments, as shown in Figure 5.

As shown in Tomassetti et al. (2016) and Ceverino et al. (2015), blue nuggets tend to display complicated rotation patterns, which are preferentially oriented along the minor axis. Indeed, we often observe multi-component misaligned, although not purely minor-axis, rotational patterns in our velocity fields (see section 4.1.2). We have confirmed that these complex velocity features are real physical features as opposed to erroneous detections by careful investigation of the flat-fielding (see section A.6.1) and by comparison between observations by different instruments (see Figure 5).

To quantify the exact magnitude and angle of the misalignment observed in our velocity fields, we interpret the complex velocity fields as consisting of two velocity "dipoles." To identify the outer dipole corresponding to the bulk rotational motion of the galaxy, we first smooth

our velocity fields with a 2D median filter with kernel size 5 pixels in order to remove any spurious line fits or high frequency noise in the data. Identifying the bulk rotation is then simply a matter of finding the two positions in the galaxy with the largest velocities. From these, we derive an angle and a maximum velocity for the outer rotation component. In order to quantify uncertainty on this metric, we perform 2D bootstrapping method allowing the exact values of the velocity in each spaxel to vary randomly within a Gaussian with σ equal to its centroiding error. We find that the error in the velocity peak positions is generally on order ~ 1 arcseconds. The error on the min/max velocity difference is typically on order ~ 5 km/s.

3.1.2. *Continuum and Line Flux Maps*

We find continuum maps readily reveal any double nuclei, if present. The continuum level of the galaxy is simply proportional to the vertical offset I_{cont} in our Gaussian model (Equation 1).

The rapid star formation rates and low metallicities of the blue nugget candidates means that the Hα and [OIII] lines are significant sources of flux. As a result Hα flux maps are a promising probe of structure compared to the lower level continuum light. For a Gaussian of the generic form:

$$f(x) = \frac{F}{\sqrt{2\pi\sigma^2}} \exp\left(\frac{-(x - \mu)^2}{2\sigma^2} \right), \qquad (5)$$

where F is the flux of the curve, σ is the standard deviation, and μ is the mean, the maximum height of the peak I_{peak} is trivially obtained at $x = \mu$:

$$I_{peak} = \frac{F}{\sqrt{2\pi\sigma^2}} \exp\left(\frac{-(\mu - \mu)^2}{2\sigma^2} \right) \qquad (6)$$

Rearranging, we find the flux is given as:

$$F = \frac{I_{peak} * \sigma}{0.3989}, \qquad (7)$$

where I_{peak} and σ are given by $I_{peak_{rest}}$ and σ_{rest} from the model fit in Equation 1, and $\frac{1}{\sqrt{2\pi}} \approx 0.3989$.

As alluded to in section 3.1.1 and described in detail in section A.6.1, errors in flat-fielding the 2013B semester GMOS IFU observations can create the appearance of bifurcations in velocity fields, continuum maps, and Hα maps. Nevertheless, we observe consistencies in reductions between instruments (as in Figure 5), in addition to consistencies in double nuclei detection between DECaLS and our 3D spectroscopic data (see Figure 6).

3.2. *Classification of DECaLS Residuals*

While our 3D spectroscopy measurements do indeed reveal sufficiently separated double nuclei (i.e. they must
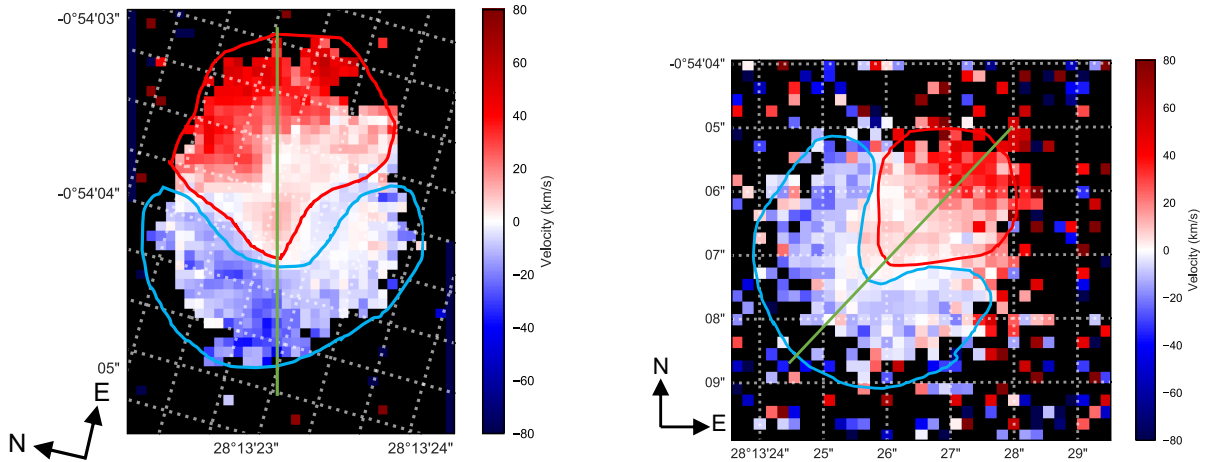
Figure 5. Independent observations of RESOLVE blue nugget candidate *rf0266* by GMOS IFU (left) and SAM FP (right) reveal consistency in data reduction and analysis methods. As a result of differences in instrument pointings, the two exposures are rotated with respect to each other, as shown by the overlaid celestial grids. Nonetheless, we find that the velocity fields display consistent features, which we emphasize. The green line denotes the photometric major axis, and the red and blue outlines trace the general shape of the kinematic features. The slight differences between the absolute celestial coordinates in the two images is the result of imprecisions in the GMOS IFU World Coordinate Solution as described in section A.9.
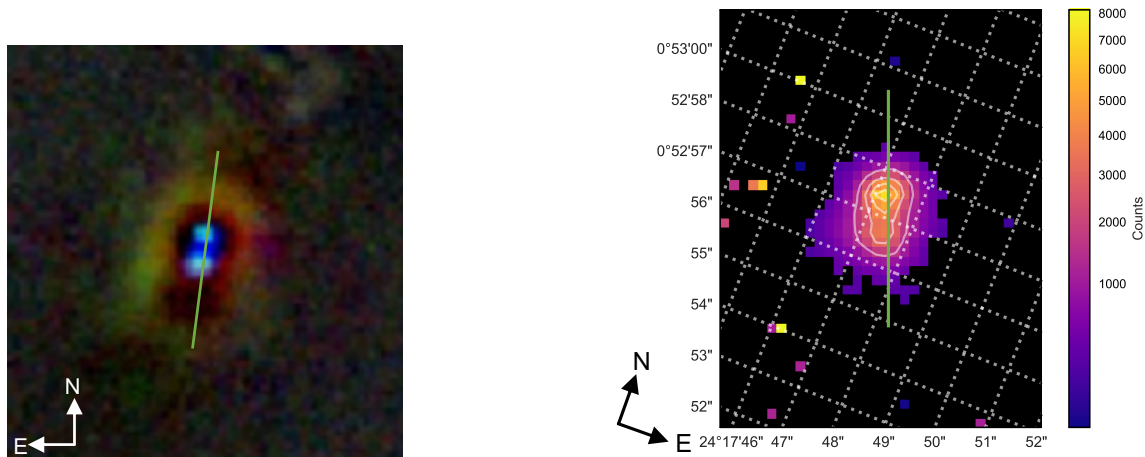
Figure 6. Double nucleus confirmation in *rf0250* further suggests consistency in the 3D spectroscopy analysis. GMOS data (right) for *rf0250* Hα emission reveal concentrations in two areas roughly aligned Northeast in agreement with the position of the nuclei observed in the DECaLS residuals (left). The green line corresponds to the approximate photometric major axis.

be separated by at least twice the spatial resolution of the observation), we only have these observations for 4 galaxies. In order to characterize the formation history (see section 4.2) of the whole blue nugget candidate population, we use by-eye classification of DECaLS DR5 residuals (see section 2.3 for a description of the data) to assign a binary 1/0 double nucleus flag to RESOLVE galaxies. A clear example of a double nucleus in the DECaLS data may be seen in Figure 6.

In order to compare the fractional occurrence rate of double nuclei, we perform our binary classification on both the blue nugget candidate population and a control population of 175 galaxies selected only on mass ($\log(M_{star}/M_\odot) < 9.5$) and morphology ($\mu_\Delta > 8.6$). In the case of both populations, in order to quantify the two-sided one-sigma confidence interval we use the IDL minimization function *AMOEBA* to find the range of possible percentages (as performed by S. Kannappan).

4. RESULTS

4.1. *Comparing the Low- and High-z samples*

Analytical modeling by Dekel & Burkert (2014) and observations of high-z blue nuggets by Barro et al. (2013) and Williams et al. (2014) have placed certain constraints and expectations on the properties of blue nuggets, including tight constraints on specific star formation rates and compactness. As described in section 2.1.2, we select our low-z blue nugget candidate sample to reflect these properties. In section 4.1.1 we examine the statistical properties of our low-z sample in relation to both other star-forming galaxies in RESOLVE (i.e. non-blue-nugget candidates with $\log$(SSFR $[Gyr^{-1}]) > -0.5$) and to the Barro et al. (2013) and Williams et al. (2014) blue nugget samples. In section 4.1.2, we examine the case for prolate morphology.

4.1.1. *Statistical Properties*

By selection, our low-z blue nugget sample has $\log$(SSFR $[Gyr^{-1}]) > -0.5$. However, star formation does not constitute the whole picture. Theory and observation have both pointed to the remarkable mass densities which accompany the fast star formation. Barro et al. (2013), Newman et al. (2012), and Williams et al. (2014) employ surface density metrics in their selection criteria, with the former two selecting objects with $\Sigma_{\alpha} = \log(M_{star}/r_e^{\alpha} [M_{\odot}kpc^{-\alpha}]) > 10.3$. They show that setting $\alpha \sim 1.5$ separates out the red and blue nuggets at $z > 1.5$. Dekel & Burkert (2014) show that this threshold corresponds to an effective stellar mass surface density of $\Sigma_s \sim 2.5 \times 10^9$ $M_{\odot}$ kpc^{-2}.

In both metrics of density, Σ_s and $\Sigma_{1.5}$, we find that our blue nugget candidates are consistently less dense than their high-z counterparts (see Figure 7). This observation is consistent with the cosmic time evolution of compactness seen by Barro et al. (2013).

4.1.2. *Prolateness and Blue Nugget Morphology*

Cosmological hydrodymical simulations (as in Ceverino et al. 2015; Tacchella et al. 2016; Tomassetti et al. 2016) have shown that the loss of angular momentum which drives the blue-nugget-forming compaction events should also create a characteristic prolate morphology. Moreover, observations by Barro et al. (2013) of blue and red nugget projected axis ratios support their hypothesized evolutionary paradigm, which suggests a morphological evolution from prolate to oblate as blue nuggets quench into quiescent red nuggets. Barro et al. (2013) suggest that the median axis ratio of $z > 1.5$ blue nuggets of $b/a \sim 0.65$ is consistent with a population displaying predominantly triaxial morphologies. Complementary observations of $z > 1.5$ red nuggets by van
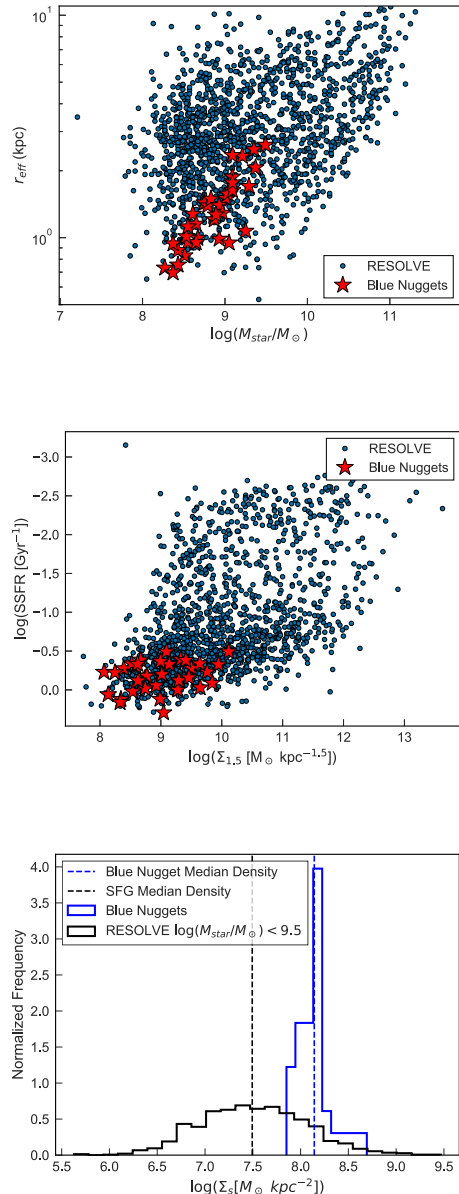
Figure 7. Top: Mass-size diagram for the low-z blue nugget candidates reveals the unique scaling relation the blue nugget candidates obey. As in the Barro et al. (2013) high-z sample, galaxies in the low-z sample consistently exhibit small radii for their mass. **Middle: Position of low-z blue nuggets in the SSFR vs. $\Sigma_{1.5}$ corroborate changes in compactness over cosmic time.** The low-z blue nugget candidates all display densities lower than those selected by Barro et al. (2013). As Barro et al. (2013) show, the compactness of star forming galaxies tend toward lower densities over cosmic time, a trend with which the low-z blue nuggets fall in line. In agreement with the redshift evolution seen in Barro et al. (2013) Figure 2, all of our blue nugget candidates fall below the $\Sigma_{1.5} < 10.3$ $M_{\odot}$ kpc$^{-1.5}$ compactness threshold used for the high-z sample while maintaining their high SSFR. **Bottom: Distribution of low-z stellar mass surface densities suggests that the low-z candidates are still unusually compact.** The low-z blue nugget candidates are on average ~ 0.65 dex more compact than other dwarf galaxies in RESOLVE.
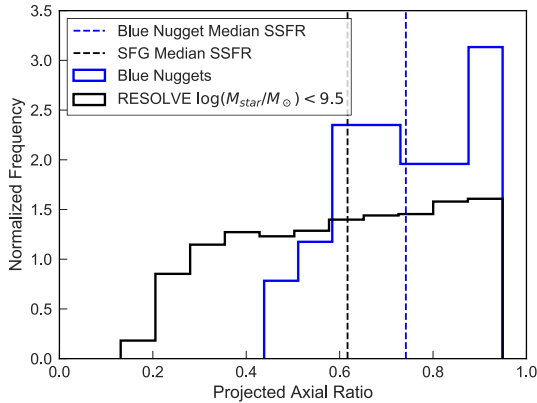
Figure 8. Distribution of blue nugget candidate projected axis ratios consistent with a preferentially prolate population. Moreover, we find that the median blue nugget candidate axis ratio of $b/a \sim 0.74$ is slightly skewed toward more spheroidal (i.e. potentially triaxial) morphologies than the Barro et al. (2013) median axis ratio of $b/a \sim 0.65$.

der Wel et al. (2011) show a slightly smaller median axis of $b/a \sim 0.54$, suggesting that some high-z red nuggets are flattened disks.

In comparison, we find a median projected axis ratio of $b/a \sim 0.74 \pm 0.03$ (see Figure 8) for our low-z blue nugget candidate sample, where the standard error is expressed as $\sigma_{med} = 1.253\frac{\sigma}{\sqrt{N}}$ (where σ is the standard deviation on b/a and N is sample size). For a control population selected only on star formation, we find a median axis ratio $b/a \sim 0.61 \pm 0.01$. However, the difference in mass selection between our sample and the Barro et al. (2013) sample likely plays a role in the notable average morphology discrepancy. As shown in van der Wel et al. (2014), the population of compact star-forming galaxies below $\log(M_{star}/M_{\odot}) \sim 9.5$ exhibits a higher prolate fraction at all redshifts $0 < z < 2$. These pieces of information together suggest that the larger median axis ratio of our low-z blue nugget candidates may be indicative of a prolate population.

4.2. *Formation of Low-z Blue Nugget Candidates*

High-z blue nuggets form as the result of fast-mode gas accretion, as described in Dekel & Burkert (2014). In the high-z universe, where cold gas mass fractions are much higher than at the present-day, either the accretion of counter-rotating cosmic streams or wet minor mergers could sufficiently maintain the requisite gas inflow rate. However, it is unclear whether both of these blue nugget formation mechanisms are still prevalent in the low-z universe. To probe the formation mechanisms of our low-z blue nugget candidate sample, we examine both the internal structures for signs of dou-

ble nuclei (section 4.2.1) and the external environments for evidence of recent or ongoing minor merger activity (section 4.2.2). In section 4.2.3, we examine our supplemental 3D spectroscopy data in comparison to the structural and kinematic predictions made in simulation (e.g. Tomassetti et al. 2016; Ceverino et al. 2015; Tacchella et al. 2016; Zolotov et al. 2015).

4.2.1. *Double Nuclei*

To constrain the frequency of double nuclei in our low-z blue nugget candidate sample, we use by-eye classification of DECaLS residuals as described in section 3.2. We find evidence for double nuclei in $85.3^{+6.2}_{-9.1}\%$ of our 35 blue nugget candidates. In a control sample consisting of 175 galaxies selected to match the candidates in mass and morphology (as in section 2.1.2), we find that $49.1^{+4.1}_{-4.0}\%$ show signs of double nuclei. However, the control sample exhibited a much higher fraction of "edge cases," compared to the relatively clear-cut classification of the blue nugget candidate sample. The difference in blue nugget fraction is further suggestive of a merger origin for the majority of blue nugget candidates. However, it remains to be seen whether colliding gas streams can also produce double nuclei. Tomassetti et al. (2016), Ceverino et al. (2015), Tacchella et al. (2016), and Zolotov et al. (2015) make no mention of double nuclei in their simulations. Likewise, Williams et al. (2014) and Barro et al. (2013) do not mention the appearance of double nuclei in their observations.

4.2.2. *Environments*

We find that the blue nugget candidates' distribution (Figure 9, left) of nearest-neighbor distances follows that of the general RESOLVE Survey for dwarf-regime galaxies ($\log(M_{star}) < 9.5$). The 90th percentile of the nearest neighbor distribution is at about 3.03 Mpc. This large distance suggests that the blue nugget candidates have preferentially formed in isolation. Moreover, the majority (27 out of 35) of blue nugget candidates lie in their own halo (i.e. the Friends-of-Friends group finding algorithm of Berlind et al. (2006) returns a "group" with group number $N = 1$). The blue nugget candidate median halo mass of $\log(M_{halo}/M_{\odot}) \sim 11.1$ further implies that the blue nugget candidates are the remnants of recent minor mergers in isolated, low-mass halos. Indeed, we observe that the majority of blue nugget candidates have M_{star}/M_{gas} ratios exceeding unity, necessitating a relatively recent source of fresh gas. (Figure 9, right)

4.2.3. *Kinematic Structure*

Our 3D spectroscopic data reveal several unique kinematic and structural features which suggest that these specific blue nugget candidates have either experienced
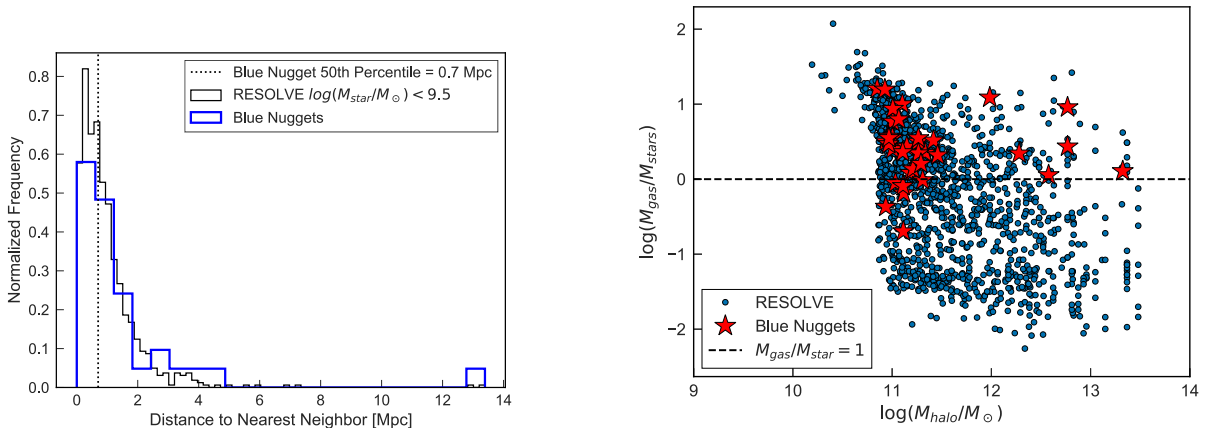
Figure 9. Distribution of blue nugget candidate nearest-neighbor distances revealing that they form in environments similar to those of other dwarf galaxies. Left: Most blue nugget candidates have formed in relative isolation. Right: The blue nugget candidates generally live in their own low-mass halo and exhibit M_{gas}/M_{star} ratios greater than unity. These data suggest that blue nuggets form in isolation as the remnants of the minor mergers which ignite their starbursts.

minor mergers in the recent past, or are currently experiencing an ongoing minor merger event. As seen in the figures in Figure 10 and Figure 11, the internal structures and dynamics of the observed blue nuggets can be quite varied and intricate.

The blue nugget candidate *rs0804* provides a very unique and informative example, as it is in the beginning stages of a minor merger. The presence of a smaller companion is immediately evident in the velocity field and Hα flux map. While the companion is just barely visible in the continuum image, the narrow spectral window of SAM FP prevents adequate sampling of a wide section of continuum. The velocity maps for this galaxy, which are re-zeroed for both the main galaxy and its companion, reveal distinct rotation patterns in each object, corroborating our claim that the two objects are distinct galaxies, rather than the smaller being a stripped off gas cloud or other similar structural anomaly.

The GMOS IFU observations of *rf0250* and *rf0266* both reveal complex, misaligned rotation structures in the velocity field. While these structures are also somewhat visible in the SAM FP observations of these galaxies, the somewhat lower SNR coupled with the slightly worse spatial resolution (due to poor seeing) of the observations reduce the detail in the maps.

In the case of the the high spatial resolution and SNR observations from the GMOS IFU, we observe two distinct rotation components misaligned from each other by about 90 degrees, which we identify by eye. Moreover, in the case of the GMOS IFU observation of *rf0250*, the positions of the double nuclei seen in the Hα flux map align with the peaks of the misaligned rotation, suggesting not only that the observed misalignment is a real, physical feature but also that it likely formed as the result of recent merger activity.

Unfortunately, the lower spatial resolution of SAM FP and SIFS coupled with the lower SNR of the SV observations prevents us from resolving any potential misaligned rotation features. Nevertheless, in the galaxies for which we have observations from multiple instruments (*rf0250* and *rf0266*) we note that the alignment of the detected double nucleus (*rf0250*) and the directions of the bulk, outer rotation are consistent between instruments.

5. DISCUSSION

Using the volume-limited RESOLVE survey, we identify a population of 35 low-redshift compact dwarf starburst galaxies analogous to high-redshift blue nuggets. We characterize the star formation, compactness, morphology, and evolutionary history relative to both the rest of the RESOLVE survey and the high-z populations observed by Barro et al. (2013) and Williams et al. (2014) and modeled by Dekel & Burkert (2014).

As a consequence of selection, blue nuggets exhibit the rigorous specific star formation rates which characterize other observational samples (e.g. Barro et al. 2013; Newman et al. 2012). However, the low-z population is deficient in stellar mass surface density by about an order of magnitude compared to both the analytical prediction performed by Dekel & Burkert (2014) and the observations by Barro et al. (2013). While it is possible that the differences in the selection criteria for the high- and low-z populations have an effect on the relative properties of the populations (namely the difference in the mass scale and the use of μ_Δ instead of a simple surface mass density metric), the lower surface mass density measurements are compatible with the redshift-evolution of compactness observed by Barro et al. (2013). Specifically, Barro et al. (2013) note that the blue nugget popula-
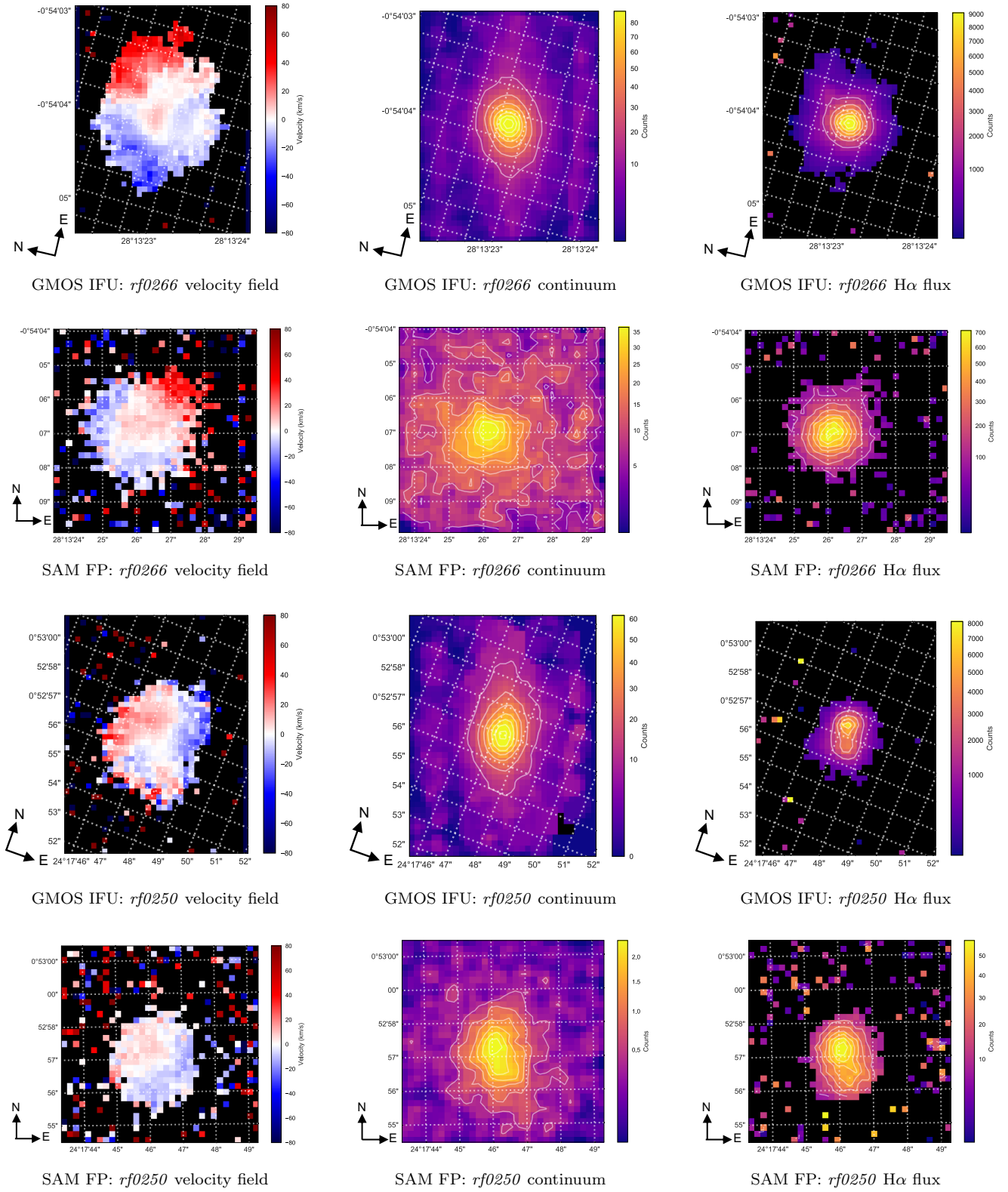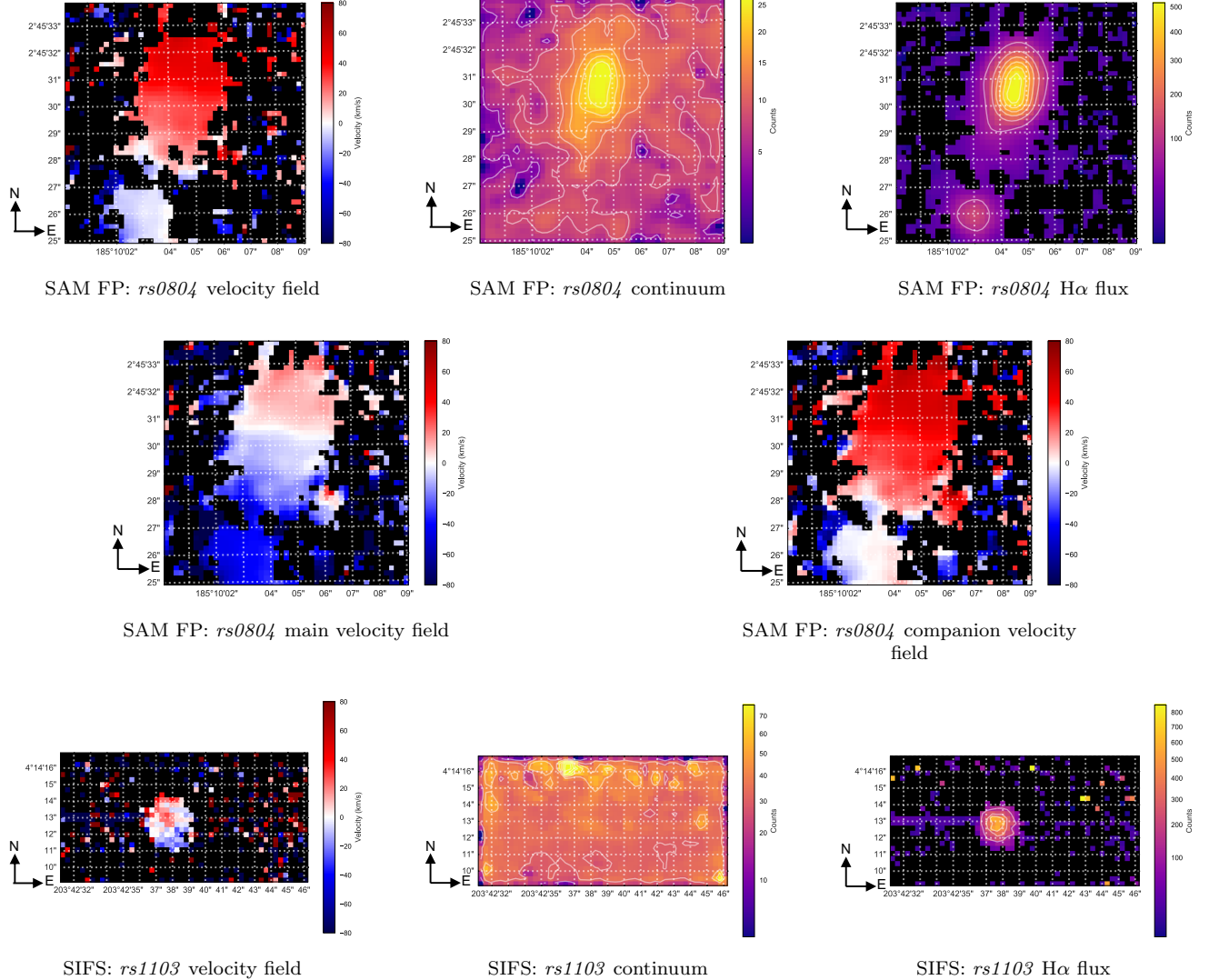
GMOS IFU: *rf0266* velocity field

GMOS IFU: *rf0266* continuum

GMOS IFU: *rf0266* Hα flux

SAM FP: *rf0266* velocity field

SAM FP: *rf0266* continuum

SAM FP: *rf0266* Hα flux

GMOS IFU: *rf0250* velocity field

GMOS IFU: *rf0250* continuum

GMOS IFU: *rf0250* Hα flux

SAM FP: *rf0250* velocity field

SAM FP: *rf0250* continuum

SAM FP: *rf0250* Hα flux

Figure 10.

SAM FP: *rs0804* velocity field

SAM FP: *rs0804* continuum

SAM FP: *rs0804* Hα flux

SAM FP: *rs0804* main velocity field

SAM FP: *rs0804* companion velocity field

SIFS: *rs1103* velocity field

SIFS: *rs1103* continuum

SIFS: *rs1103* Hα flux

Figure 11.

tion begins to steadily disappear at $z \sim 3$, before becoming nearly absent at $z < 1.4$. Moreover, the entire population of galaxies tends toward lower densities with cosmic time. However the Barro et al. (2013) sample does not probe blue nuggets with stellar mass below $\log(M_{star}/M_\odot) = 10$. In this interpretation of events, the low-z blue nugget candidates may be seen as the present-day universe analogue of blue nuggets in that they are starbursting dwarf galaxies that are notably more compact than galaxies of similar mass (Figure 7).

An important prediction of the blue nugget simulation literature is the prolate morphology seen at peak compaction (Jing & Suto 2002; Bailin & Steinmetz 2005; Allgood et al. 2006). Moreover, Tomassetti et al. (2016) and Ceverino et al. (2015) show that blue nuggets preferentially display minor-axis rotation aligned with the cosmic web structure in which they are embedded. Un-

fortunately, we cannot directly probe the intrinsic morphologies of individual blue nuggets since we observe them in projection. If we were able to observe pure minor-axis rotation in our 3D spectroscopic velocity fields, it would be possible to infer prolate morphology from this. However, we do not observe pure minor axis rotation in any of the four galaxies for which we have follow-up 3D spectroscopy. Nonetheless, we are able to statistically characterize the projected axis ratio of the low-z blue nugget candidate population. Interestingly, we observe a median projected axis ratio of $b/a \sim 0.74$, compared to the Barro et al. (2013) measurement of $b/a \sim 0.65$, suggesting that our sample may be skewed slightly more toward triaxial (i.e. prolate) morphologies as a population.

Rather than pure minor axis rotation, we do observe multi-component, misaligned rotation in our 3D spec-

troscopic velocity fields, especially in the case of *rf0250* and *rf0266*. Moreover, the positions of the double nuclei detected in *rf0250* align with the peaks of the inner velocity structure. This fact not only provides further evidence that the bifurcated velocity structure is physical, and not a calibration effect, but also is extremely suggestive of a recent minor merger. In fact, we observe evidence of double nuclei in DECaLS residuals for a whopping $\sim 85\%$ of our blue nugget candidate sample, compared to $\lesssim 49\%$ in a control population selected to resemble blue nugget candidates in mass and morphology. This observation highly favors a minor merger scenario for the majority of the low-z sample.

The high gas-to-stellar-mass ratios observed in the RESOLVE blue nugget candidates requires a recent source of fresh gas. As suggested by the high frequency of double nuclei observed in the sample and by the complex kinematics seen in the 3D spectroscopy observations, fresh gas accretion is likely occurring through wet minor mergers. However, the discrepancy in compactness observed between the high-z and low-z samples suggests that the RESOLVE blue nugget candidates may not be blue nuggets in the truest sense of the term. Rather, our low-z blue nugget candidate sample may constitute a modern "tail" of the blue nugget evolution story, which is transitioning to a different mode of growth distinct from the fast-mode growth observed at high redshift. In this interpretation, our low-z blue nugget candidates are not true blue nuggets but rather a transitional population of galaxies situated between high-z blue nuggets and low-z normal galaxies. As an intermediary between these populations, they retain many of the aspects of blue nuggets (large specific star formation rates, color, compactness relative to similarly massive galaxies at similar redshifts, etc.), but may be more like normal galaxies in that they may form disks and other structural features typically associated with modern-day galaxies.

Kannappan et al. (2013) show that gas-dominated galaxies become typical of the blue sequence below $M_{star} \sim 10^{9.5} - 10^{10}$ M$_\odot$ (the so-called "gas-richness threshold scale") in the low-z universe. Indeed, we find our gas-rich blue nugget candidates below the threshold scale. However, extreme compactness of our candidates relative to other RESOLVE galaxies demands a mechanism allowing for such a rapid bulge growth. As evidenced by the high double nucleus fraction and the complex kinematics seen in the 3D spectroscopy observations, the mechanism for bulge growth is occurring dominantly via wet minor mergers at the present epoch. Nevertheless, these present-day wet minor mergers cannot reproduce the same compactnesses measured

for high-redshift galaxies, suggesting that the RESOLVE blue nugget candidates have evolved along neither the "fast-track" or "slow-track" paths detailed in Dekel & Burkert (2014). Rather, we suggest that our blue nugget candidates may have evolved along an intermediary "accelerated-track."

The inaccessibility of fast-track evolution in the low-z universe may result from the lower cold gas mass inventory and lower merger rate at the present-day. Moreover, we observe that most blue nugget candidates have formed in relatively extreme isolation as the sole member of their own low-mass halo (see Figure 9). Essentially, these factors make it more difficult to produce incredibly compact objects as cosmic time progresses, as suggested by the trend in decreasing compactness demonstrated by Barro et al. (2013) that continues into the present epoch (as seen in Figure 7, middle).

Interestingly, accelerated-mode evolution leaves open the possibility of disk regrowth following the starburst stage observed in the low-z blue nugget candidate population. Stark et al. (2013) show that galaxies in the low-z universe should evolve along a triangle-shaped "fueling diagram" which relates global H_2/HI and mass-corrected blue-centeredness. Specifically they demonstrate that galaxies on the right branch of their fueling diagram, which contains blue-sequence E/S0s and blue compact dwarfs (BCDs), have likely formed via gas-rich mergers between galaxies of similar mass. The double nucleus, environmental, and kinematic data for blue nuggets point precisely toward this scenario, suggesting that the low-z blue nugget candidates may share similar evolutionary histories as the right-branch galaxies. Indeed, subsequent molecular gas observations might reveal that the present-day blue nugget candidates fall on the right branch given the properties and potential evolutionary histories they share with blue E/S0s.

Stark et al. (2013) show that the bottom-branch galaxies in the fueling diagram have properties consistent with right-branch galaxies (e.g. stellar mass, gas richness, numerous blue E/S0s, etc.) but exhibit depressed H_2/HI ratios as they evolve leftward along the diagram. However, Stark et al. (2013) show that there is a general *increase* in the total gas-to-stellar-mass ratio as the bottom-branch galaxies decrease in mass-corrected blue-centeredness. They ultimately conclude that this trend is consistent with outer-disk building and the eventual formation of visible spiral arms. The presence of this evolutionary path in the low-z universe combined with the slower "accelerated-mode" growth which we infer for our RESOLVE blue nugget candidates suggests that our blue nugget candidates have the potential to evolve into normal higher-mass galaxies, as opposed to their

high-z counterparts which preferentially quench into red nuggets after hot-halo quenching rapidly shuts down star formation and fresh gas accretion.

Accounting for all factors, we note that our population of low-z blue nuggets resembles the high-z population in their high specific star formation rates, low masses, and extreme compactness relative to galaxies of similar masses. Moreover, the distribution of their projected axis ratios is compatible with a population skewed more toward triaxial (and potentially prolate) morphologies relative to the Barro et al. (2013) sample. Nonetheless, the low-z blue nugget candidates are notably less compact than their high-z counterparts, by as much as a dex in stellar surface mass density. As such, our low-z blue nugget candidate sample likely consists of the modern universe's analogue to high-z blue nuggets. Barro et al. (2013) demonstrate that on average galaxies, including blue and red nuggets, consistently decrease in density with cosmic time. With this in mind, we conclude that our sample, while perhaps not bona fide blue nuggets, exhibit specific star formation rates, morphologies, and formation mechanisms akin to blue nuggets, and therefore may be conservatively recognized as low-z blue nugget *analogues*.

6. CONCLUSIONS

In this work, we aimed to explore the existence, properties, and formation of low-z blue nugget analogues in the RESOLVE survey, a volume-limited census of galaxies in the local universe.

- To identify a population of low-z galaxies analogous to high-z blue nuggets, we implement selectors in mass, morphology, color, and star formation (Figure 2), yielding a population of 35 RESOLVE galaxies. Comprising about ∼ 1.5% of the galaxies in RESOLVE, these objects represent some of the most compact, blue, and star forming galaxies in the survey.

- We compare the statistical properties of our low-z sample with the observed and simulated characteristics of high-z blue nuggets using various ancillary RESOLVE data. We find that the low-z sample exhibits a similar distribution of specific star formation rates to the high-z sample (by selection), shows a distribution of projected axis ratios suggestive of prolate morphology, and demonstrates notable compactness relative to galaxies of the same mass at the same redshift. However, the low-z population is on average less dense than the typical high-z sample by about a dex.

- By-eye classification of the low-z blue nugget candidate population and a control population selected on mass and morphology has revealed that low-z blue nuggets are much more likely to host resolved double nuclei. We find that ∼ 85% of RESOLVE blue nugget candidates have visible double nuclei in the DECaLS DR5 residuals, compared to ≲ 49% for the control sample selected to resemble the blue nugget candidates in mass and morphology.

- We find that the distribution of nearest-neighbor distances for the low-z blue nugget candidates follows that of the general RESOLVE survey (Figure 9, left). Moreover, the typically low halo masses (Figure 9, right) coupled with the high fraction of double nuclei presence suggests that the majority of blue nuggets form as the result of wet minor mergers in their own small halos. This evolutionary picture is narratively consistent with merger mechanism of angular momentum loss and compaction proposed in high-z simulation, such as in Zolotov et al. (2015) and Tomassetti et al. (2016).

- Follow-up 3D spectroscopy with the GMOS IFU, SAM FP, and SIFS has revealed the complex inner workings of four of the low-z blue nugget candidate galaxies. In the case of *rf0250* and *rf0266*, we directly detect double nuclei as well as a characteristic "misaligned" rotation pattern. The peaks of the inner rotation align with the double nuclei position, suggesting a merger origin for these galaxies.

- We speculate that the low-z blue nugget analogues evolve in an "accelerated-mode" which leaves open the possibility for subsequent disk regrowth and evolution into normal galaxies (as opposed to quenched red nuggets) as suggested by the Stark et al. (2013) fueling diagram.

In total, we have demonstrated that a highly unique class of galaxies at high redshift – blue nuggets – have analogues in the present-day universe. These low-z blue nugget analogues suggest that the violent compaction events which drove rapid galaxy evolution and star formation in the early universe still exist to some extent at the present epoch.

APPENDIX

A. THE GEMINI REDUCTION PIPELINE

The ultimate goal of the Gemini Reduction Pipeline is to transform raw 2D scientific and calibration exposures into a 3D data cube, that contains spatial data on the xy-plane and spectral data on the z-axis. To do so, the Pipeline uses the GMOS IRAF package[5], which contains a variety of tasks designed to aid in the reduction process. The GMOS IRAF tasks are tailored for use with Gemini instruments, which store raw data as Multiple-Extension FITS (MEF) files. The Pipeline itself is a long Python script which sequentially calls the GMOS reduction tasks with the proper inputs.

The Pipeline is designed to run in a working directory initially containing the raw data, obtained from the Gemini Observatory Archive, and a handful of calibration files (e.g. a bias frame and a file containing a list of strong lamp lines used in the wavelength calibration step). At each step in the reduction process, the Pipeline writes out a new file with a prepended identifying letter, rather than overwriting the input files.

A.1. *Pre-reduction Tasks*

Before the Pipeline can perform the reduction of the scientific data of interest, we must perform several miscellaneous tasks to create the calibration files the Pipeline later uses in the processing of the scientific data. The two major tasks required are the creation of a bias frame (section A.1.1) and the creation of the sensitivity function from the standard star data (section A.1.2).

A.1.1. *Creation of the Bias Frame*

Early in the reduction process, the Pipeline performs a bias subtraction of the flat, arc, and science frames. To perform this step, a single bias frame must be constructed from the five bias frames taken before the start of the night. Outside the Pipeline, this task is performed using the GMOS IRAF task *gbias*, which subtracts and trims the overscan regions (the parts of the detector array where no light falls) before combining the individual biases.

#### A.1.2. *Reduction of the Standard Star Data*

In order to flux calibrate the scientific data, the Pipeline uses a sensitivity function which defines the conversion ratio between Analog-to-Digit Units (ADUs) and physical flux in each pixel. The sensitivity function files are produced by a "mini-reduction" which is largely analogous to the scientific reduction process, but with a few added steps. The Standard Star Reduction Pipeline is used to perform the mini-reduction, which culminates with the creation of a summed 1D spectrum of the standard star. Since the standard star's flux as a function of wavelength is well-known, the Pipeline is able to compare the known flux with the ADU count at each wavelength to compute the sensitivity function. If the scientific observations consist of multiple wavelength dithers, a sensitivity function will be created for each.

A.2. *First Steps and Initial Calibrations*

Before performing any actual reduction, the Pipeline first identifies and sorts the raw files in the working directory. This step is quite simple: the Pipeline loops over the files with the correct name convention ("S*.fits"), opening them, and sorting them using the "obsclass" keyword in the FITS headers.

---

[5] http://www.gemini.edu/sciops/data-and-results/processing-software

With the files sorted, the Pipeline perform three initial calibrations on the flats, which are used to both flat-field the scientific data and identify the fibers. The first step of the flat reduction is the creation of a "Mask Definition File" (MDF), which is appended (or "attached") as a new extension to each MEF file. The MDF defines the sky coordinates of each fiber on the CCD, which allow the Pipeline to remap the 2D detector data into a 3D cube later in the reduction. To define and attach the MDF, we use the GMOS IRAF task *gfreduce* on the dome flat images. The task *gfreduce* can perform many different reduction procedures, but here we simply use it to perform the initial calibrations of the flats. The MDF defines bad fibers of the instrument, which we are required to verify by manually checking the results of the automated fiber identification. Figure 12 shows an example fiber identification window.
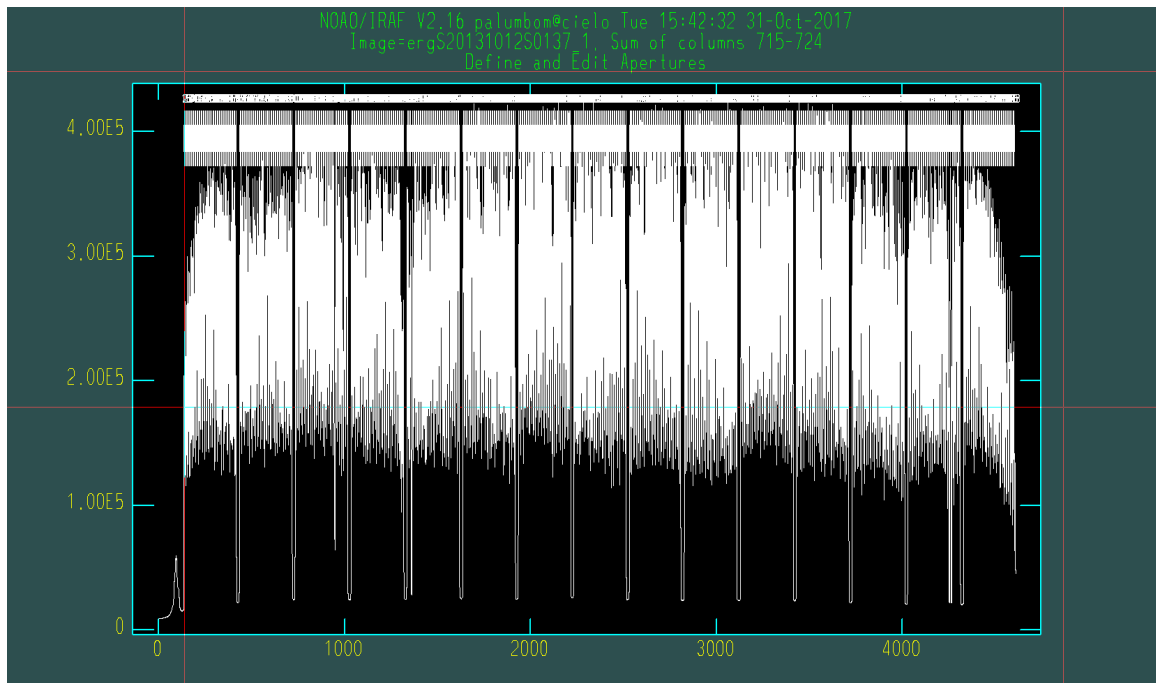
Figure 12. Example fiber identification window. Each "bundle" of lines is a fiber bundle consisting of 50 fibers. The numeric ID assigned to each fiber by *gfreduce* must be manually checked. Incorrectly identifying the fibers can prevent proper data cube creation.

gfreduce now handles the bias subtraction and overscan subtraction and trimming of the flats. The overscan regions correspond to portions of the CCD array where light does not fall. We therefore must subtract the counts in these regions from the rest of the data and then trim them from the images.

The Pipeline repeats the above procedure of MDF attachment, overscan subtraction, and trimming for the lamp arcs. Since the arc readout speed is much faster than for the other data, we cannot use the usual bias frame to perform the bias subtraction here. Instead, we rely on the overscan levels as a rough estimate as the bias level. Finally, the Pipeline performs the bias and overscan subtraction of the science frames, as for the flats.

A.3. *Bad Pixel Identification and Interpolation*

The Pipeline then prompts the creation of a "Bad Pixel Mask" (BPM), if one has not already been made. A BPM is simply a FITS file which marks pixel quality with a boolean flag. Bad pixels can be identified by eye by examining the trimmed and bias-subtracted science files prepared in the previous step. Bad pixels do not include cosmic ray hits, which are identified and removed in a later step (section A.6). Since bad pixels generally change quite slowly, one BPM can often be used for any observation in the same semester. Once created, the Pipeline uses the task *addbpm* to attach the BPM to the data file, and then uses *gemfix* to attach data quality extensions to each MEF and interpolate over the bad pixels in the science, flat, and arc images.

A.4. *Arc Extraction and Wavelength Solution Creation*

The Pipeline then uses the task *gfextract* to extract the arc spectra using the fiber IDs created from the flats in the first step. Now, the Pipeline calls the task *gswavelength*, which creates a wavelength solution for the arc frames. This task compares each extracted spectrum to a provided list of strong emission lines and makes a polynomial fit to the data. In order to obtain a robust wavelength solution, we require that the RMS of each fit be below ~ 0.09. Once the wavelength solution has been created, the Pipeline uses *gftransform* to apply the solution to the arc lamp images.

A.5. *Quantum Efficiency Correction, Flat-Fielding, and Wavelength Solution Redo*

The Pipeline now performs quantum efficiency (QE) correction on the flats using *gqecorr*, and then re-extracts the BPM- and QE-corrected flat spectra. With these steps completed, the Pipeline, with *gfresponse*, now uses the re-extracted flats and the twilight twilight flats to create the response function which will be used to flat-field the arc lamp and science data. The response function will correct for three factors: pixel-to-pixel variations in the CCD, the wavelength-dependent efficiency of the pixels, and illumination variations.

The Pipeline uses *gqecorr* on the arcs, and then applies the response function created in the previous step to the now QE-corrected arcs using *gfreduce*. The QE correction step changes the pixel values in the arcs, which necessitates the recreation of the wavelength solution. The wavelength solution redo is performed identically as before, using *gswavelength* to make the solution, and then *gftransform* to apply the new solution to the arcs. Figure 13 shows example wavelength-transformed science data.
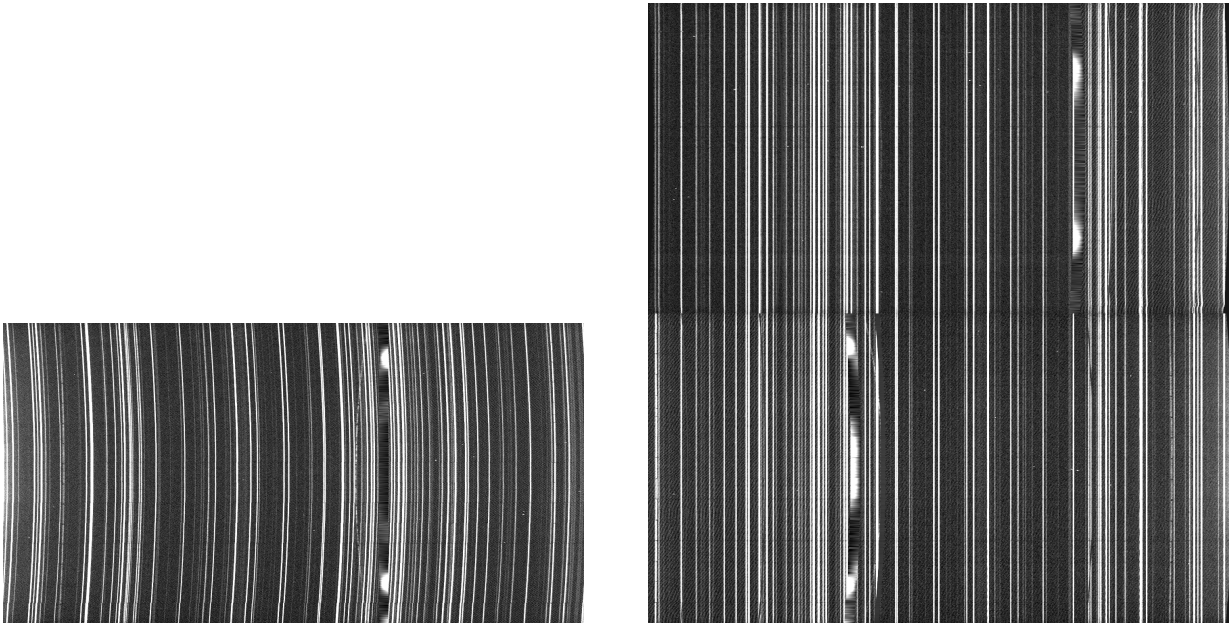

Figure 13. At left: Copper-Argon (CuAr) arc lamp spectrum prior to the wavelength transformation. Note the curved emission lines on the detector. **At right:** CuAr arc lamp spectrum after performing the wavelength transformation. The curved emission lines are now straight. Jagged or curved lines would indicate a bad wavelength solution. The change in image dimension between the untransformed and transformed images is the result of *gftransform* stitching together the data from each chip amplifier into a single image.

A.6. *Calibration of the Scientific Data*

With the arcs re-transformed, the Pipeline's processing of the calibration data has finished. The final steps of the reduction apply these calibrations to the science frames and map the 2D science data to 3D data cubes. The Pipeline first uses PyCosmic[6] (Husemann et al. 2012) to identify and scrub cosmic rays from the science spectra. PyCosmic uses the same Laplacian edge detection method as L.A. Cosmic (van Dokkum 2001), but with various extensions to

---

[6] http://www.bhusemann-astro.org/?q=pycosmic
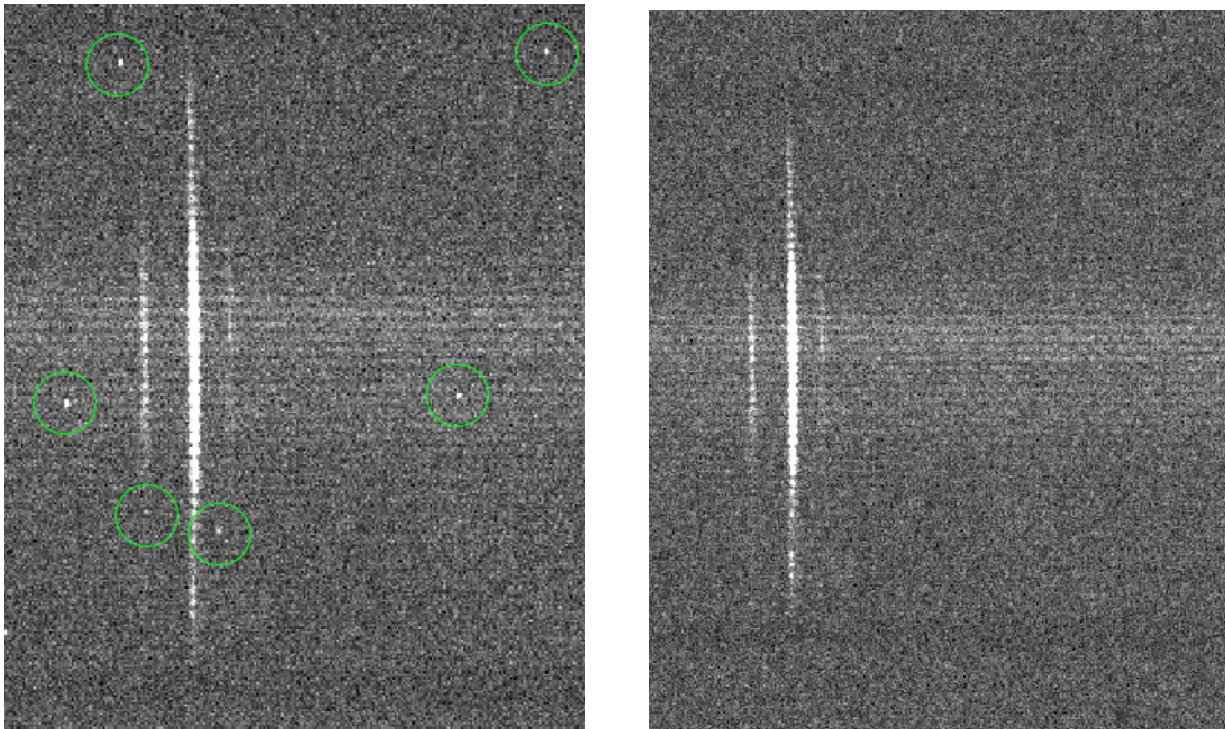
Figure 14. Example fiber spectra before (left) and after (right) cosmic ray removal. PyCosmic has effectively removed the cosmic ray hits (circled in green) without harming the delicate scientific data.

the algorithm specifically tailored for use with fiber-fed spectrograph data. Whereas L.A. Cosmic frequently falsely construes the bead-like structure of the fiber data as cosmic ray hits, PyCosmic is better able to differentiate the scientific data and therefore avoids destruction of strong emission lines, such as Hα. Following cosmic ray removal, the Pipeline then applies the response function and the wavelength solution to the science spectra by using *gfreduce* and *gftransform* in succession.

A.6.1. *Improper Flat-fielding and the "Two-slit" Issue*

Unfortunately, observations in the Gemini program GS-2013B-Q-51 consistently lack twilight flats in one of the wavelength dithers. Therefore, we are unable to create a response function to properly flat-field any observations in the redder wavelength dither. Moreover, without proper flat-fielding, the differential throughput of the pseudoslits is unaccounted for. Unfortunately, this "two-slit issue" can create a false bifurcation in the final scientific data cube (see section A.8) which may persist in the velocity fields, continuum, and line flux maps described in section 3.1.1 and section 3.1.2. Unfortunately, we have only managed to free ourselves from the two-slit issue by excluding the red dither exposures in the 2013B semester from the data cube creation step. Consequently, these observations have SNR reduced by a factor of $\sqrt{2}$. In section 3.1.1, we show that consistency between GMOS IFU red dither data and SAM FP data suggest that any double nuclei and velocity field misalignment features are genuine physical features, as opposed to calibration effects.

A.7. *Sky Subtraction and Flux Calibration of Science*

The pipeline now performs the sky subtraction of the science data. Since several prominent sky lines exist in the wavelength range of interest, proper sky subtraction is of extreme importance. Since a few hundred fibers in the IFU are dedicated to sky sampling (i.e. they fall off-object on blank sky), we use these fibers to sample the sky spectrum. The identification and subtraction of sky spectra is performed with *gfskysub*. As a final step before data cube creation, the Pipeline uses the response function files (created in the standard star reduction) to flux calibrate the science data. This sensitivity function is applied to the science data using *gscalibrate*.

$\lambda \sim 6686$ Å $\lambda \sim 6687$ Å $\lambda \sim 6688$ Å
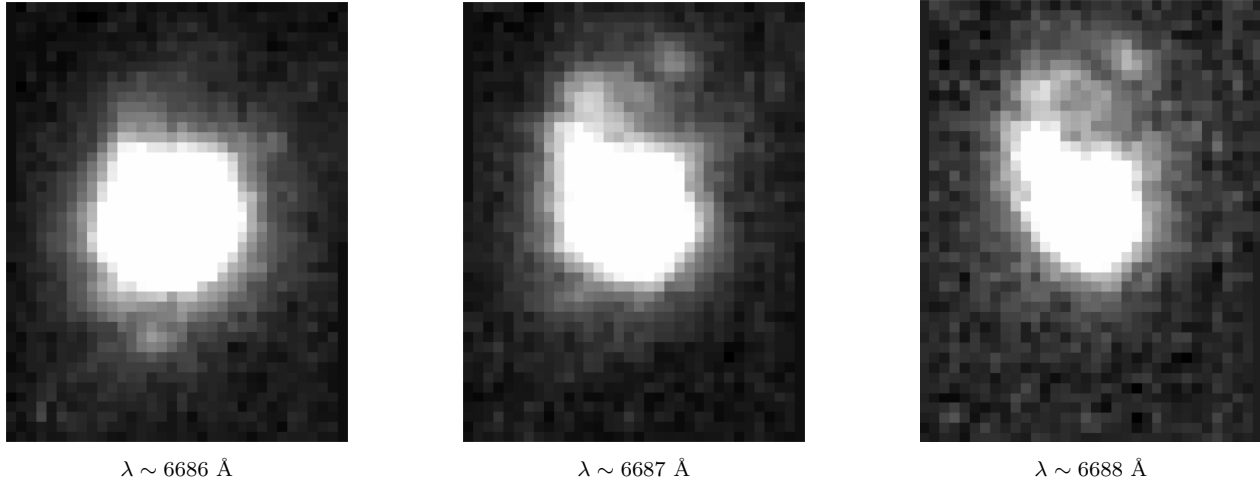
Figure 15. Slices of the assembled data cube for *rf0266* sampled at three points on the redshifted Hα line suggest complex kinematics. We later use the shape and position of this line to extract a velocity map of the galaxy from the data cube. See section 3.1.1.

A.8. *Data Cube Creation and Mosaicking*

At this point in the reduction, the Pipeline resamples the science spectra into data cubes using *gfcube*. This step produces a data cubes for every science exposure. For blue nugget observations, there are generally four science exposures (two spatial and two spectral offsets). The Pipeline then combines the separate data cubes into a single, final cube. To perform this step, the Pipeline uses the PyFu package[7] written by Gemini staff member James Turner. The actual merging of the cubes is performed in a two step process. First, the PyFu task *pyfalign* makes a centroid fit over the brightest feature in each wavelength-summed cube and calculates the spatial offsets of the centroid in each region. With the spatial offsets quantified, the *pyfmosaic* task resamples the cubes onto a common grid and then co-adds them. Any bad pixels noted in the data quality extension of the MEF are ignored in this step.

A.9. *WCS Creation*

Finally, the Pipeline creates a World Coordinate Solution (WCS) for the merged data cube. The known pixel scale σ of the scientific data and rotation θ of the final acquisition image are used to calculate the FITS CD matrix given by:

$$\begin{pmatrix} \text{CD1\_1} & \text{CD1\_2} \\ \text{CD2\_1} & \text{CD2\_2} \end{pmatrix} = \sigma \begin{pmatrix} \cos\theta & \sin\theta \\ -\sin\theta & \cos\theta \end{pmatrix} \tag{A1}$$

The RA and DEC coordinates of the reference pixel are calculated as an offset, which depends on both the disperser used and the semester of the observation, from the commanded telescope pointing. However, the actual and commanded pointings vary with respect to each other by up to a few arcminutes. So while the rotation and scale of the WCS are well-determined, the WCS reference coordinate tends to be quite inaccurate. Normally, the WCS reference coordinate could be improved by calculating the offsets of field stars in the image, but the small field-of-view of our blue nugget observations does not contain any. To compensate for this issue, we manually change the coordinates of the reference pixels to center on the object.

---

[7] http://drforum.gemini.edu/topic/pyfu-datacube-mosaicking-package/

REFERENCES

Aihara, H., Allende Prieto, C., An, D., et al. 2011, The Astrophysical Journal Supplement Series, 193, doi: 10.1088/0067-0049/193/2/29

Allgood, B., Flores, R. A., Primack, J. R., et al. 2006, MNRAS, 367, 1781, doi: 10.1111/j.1365-2966.2006.10094.x

Bailin, J., & Steinmetz, M. 2005, ApJ, 627, 647, doi: 10.1086/430397

Barro, G., Faber, S. M., Pérez-González, P. G., et al. 2013, ApJ, 765, doi: 10.1088/0004-637X/765/2/104

Berlind, A. A., Frieman, J., Weinberg, D. H., et al. 2006, The Astrophysical Journal Supplement Series, 167, 1, doi: 10.1086/508170

Bonnarel, F., Fernique, P., Bienaymé, O., et al. 2000, Astronomy and Astrophysics Supplement Series, 143, 33, doi: 10.1051/aas:2000331

Ceverino, D., Primack, J., & Dekel, A. 2015, MNRAS, 453, 408, doi: 10.1093/mnras/stv1603

Chang, Y.-Y., van der Wel, A., Rix, H.-W., et al. 2013, ApJ, 773, doi: 10.1088/0004-637X/773/2/149

Codis, S., Pichon, C., & Pogosyan, D. 2015, MNRAS, 452, 3369, doi: 10.1093/mnras/stv1570

Colless, M., Dalton, G., Maddox, S., et al. 2001, MNRAS, 328, 1039, doi: 10.1046/j.1365-8711.2001.04902.x

Damjanov, I., Zahid, H. J., Geller, M. J., & Hwang, H. S. 2015, ApJ, 815, doi: 10.1088/0004-637X/815/2/104

Damjanov, I., McCarthy, P. J., Abraham, R. G., et al. 2009, ApJ, 695, 101, doi: 10.1088/0004-637X/695/1/101

Dekel, A., & Burkert, A. 2014, MNRAS, 438, 1870, doi: 10.1093/mnras/stt2331

Driver, S. P., Hill, D. T., Kelvin, L. S., et al. 2011, MNRAS, 413, 971, doi: 10.1111/j.1365-2966.2010.18188.x

Eckert, K. D., Kannappan, S. J., Stark, D. V., et al. 2016, ApJ, 824, doi: 10.3847/0004-637X/824/2/124

—. 2015, ApJ, 810, doi: 10.1088/0004-637X/810/2/166

Eggen, O. J., Lynden-Bell, D., & Sandage, A. R. 1962, ApJ, 136, 748, doi: 10.1086/147433

Falco, E. E., Kurtz, M. J., Geller, M. J., et al. 1999, Publications of the Astronomical Society of the Pacific, 111, 438, doi: 10.1086/316343

Hambly, N. C., Collins, R. S., Cross, N. J. G., et al. 2008, MNRAS, 384, 637, doi: 10.1111/j.1365-2966.2007.12700.x

Haynes, M. P., Giovanelli, R., Martin, A. M., et al. 2011, AJ, 142, doi: 10.1088/0004-6256/142/5/170

Hogg, D. W., & Lang, D. 2013, Publications of the Astronomical Society of the Pacific, 125, 719, doi: 10.1086/671228

Hopkins, P. F., Cox, T. J., & Hernquist, L. 2008, ApJ, 689, doi: 10.1086/592105

Hunter, J. D. 2007, Computing in Science and Engineering, 9, 90, doi: 10.1109/MCSE.2007.55

Husemann, B., Kamann, S., Sandin, C., et al. 2012, A&A, 545, doi: 10.1051/0004-6361/201220102

Ilbert, O., Salvato, M., Le Floc'h, E., et al. 2010, in SF2A-2010: Proceedings of the Annual meeting of the French Society of Astronomy and Astrophysics. Eds.: S. Boissier, M. Heydari- Malayeri, R. Samadi and D. Valls-Gabaud, p.355, 355

Jing, Y. P., & Suto, Y. 2002, ApJ, 574, 538, doi: 10.1086/341065

Jones, D. H., Read, M. A., Saunders, W., et al. 2009, MNRAS, 399, 683, doi: 10.1111/j.1365-2966.2009.15338.x

Kannappan, S. J., Fabricant, D. G., & Franx, M. 2002, AJ, 123, 2358, doi: 10.1086/339972

Kannappan, S. J., & Gawiser, E. 2007, ApJ, 657, L5, doi: 10.1086/512974

Kannappan, S. J., Stark, D. V., Eckert, K. D., et al. 2013, ApJ, 777, doi: 10.1088/0004-637X/777/1/42

Khochfar, S., & Silk, J. 2006, ApJ, 648, L21, doi: 10.1086/507768

Laigle, C., Pichon, C., Codis, S., et al. 2015, MNRAS, 446, 2744, doi: 10.1093/mnras/stu2289

Lang, D., Hogg, D. W., & Mykytyn, D. 2016, The Tractor: Probabilistic astronomical source detection and measurement, Astrophysics Source Code Library. http://ascl.net/1604.008

Law, D. R., Steidel, C. C., Shapley, A. E., et al. 2012, ApJ, 745, doi: 10.1088/0004-637X/745/1/85

Markwardt, C. B. 2009, in Astronomical Data Analysis Software and Systems XVIII ASP Conference Series, Vol. 411, proceedings of the conference held 2-5 November 2008 at Hotel Loews Le Concorde, Québec City, QC, Canada. Edited by David A. Bohlender, Daniel Durand, and Patrick Dowler. San Francisco: Astronomical Society of the Pacific, 2009., p.251, Vol. 411, 251

McCall, M. L. 2004, AJ, 128, 2144, doi: 10.1086/424933

Mendes de Oliveira, C., Amram, P., Quint, B. C., et al. 2017, MNRAS, 469, 3424, doi: 10.1093/mnras/stx976

Moffett, A. J., Kannappan, S. J., Berlind, A. A., et al. 2015, ApJ, 812, doi: 10.1088/0004-637X/812/2/89

Morrissey, P., Conrow, T., Barlow, T. A., et al. 2007, The Astrophysical Journal Supplement Series, 173, 682, doi: 10.1086/520512

Naab, T., Johansson, P. H., Ostriker, J. P., & Efstathiou, G. 2007, ApJ, 658, 710, doi: 10.1086/510841

Naab, T., & Ostriker, J. P. 2009, ApJ, 690, 1452, doi: 10.1088/0004-637X/690/2/1452

Nelson, E., van Dokkum, P., Franx, M., et al. 2014, Nature, 513, 394, doi: 10.1038/nature13616

Newman, A. B., Ellis, R. S., Bundy, K., & Treu, T. 2012, ApJ, 746, doi: 10.1088/0004-637X/746/2/162

Newman, A. B., Ellis, R. S., Treu, T., & Bundy, K. 2010, ApJ, 717, L103, doi: 10.1088/2041-8205/717/2/L103

O'Donnell, J. E. 1994, ApJ, 422, 158, doi: 10.1086/173713

Patel, S. G., van Dokkum, P. G., Franx, M., et al. 2013, ApJ, 766, doi: 10.1088/0004-637X/766/1/15

Paturel, G., Petit, C., Prugniel, P., et al. 2003, A&A, 412, 45, doi: 10.1051/0004-6361:20031411

Skrutskie, M. F., Cutri, R. M., Stiening, R., et al. 2006, AJ, 131, 1163, doi: 10.1086/498708

Stark, D. V., Kannappan, S. J., Wei, L. H., et al. 2013, ApJ, 769, doi: 10.1088/0004-637X/769/1/82

Stark, D. V., Kannappan, S. J., Eckert, K. D., et al. 2016, ApJ, 832, doi: 10.3847/0004-637X/832/2/126

Tacchella, S., Dekel, A., Carollo, C. M., et al. 2016, MNRAS, 457, 2790, doi: 10.1093/mnras/stw131

The Astropy Collaboration, Price-Whelan, A. M., Sipócz, B. M., et al. 2018, ArXiv e-prints. https://arxiv.org/abs/1801.02634

Toft, S., van Dokkum, P., Franx, M., et al. 2007, ApJ, 671, 285, doi: 10.1086/521810

Tomassetti, M., Dekel, A., Mandelker, N., et al. 2016, MNRAS, 458, 4477, doi: 10.1093/mnras/stw606

Trujillo, I., Conselice, C. J., Bundy, K., et al. 2007, MNRAS, 382, 109, doi: 10.1111/j.1365-2966.2007.12388.x

van der Wel, A., Rix, H.-W., Wuyts, S., et al. 2011, ApJ, 730, doi: 10.1088/0004-637X/730/1/38

van der Wel, A., Chang, Y.-Y., Bell, E. F., et al. 2014, ApJ, 792, doi: 10.1088/2041-8205/792/1/L6

van Dokkum, P. G. 2001, Publications of the Astronomical Society of the Pacific, 113, 1420, doi: 10.1086/323894

van Dokkum, P. G., Franx, M., Kriek, M., et al. 2008, ApJ, 677, doi: 10.1086/587874

Warren, M. S., Abazajian, K., Holz, D. E., & Teodoro, L. 2006, ApJ, 646, 881, doi: 10.1086/504962

Williams, C. C., Giavalisco, M., Cassata, P., et al. 2014, ApJ, 780, doi: 10.1088/0004-637X/780/1/1

Zolotov, A., Dekel, A., Mandelker, N., et al. 2015, MNRAS, 450, 2327, doi: 10.1093/mnras/stv740